ENN Encyclopedia of Nanoscience and Nanotechnology
www.aspbs.com/enn

Anodic Aluminum Oxide–Based Nanostructures and Devices

Chi Lu, Zhi Chen

Department of Electrical and Computer Engineering and Center for Nanoscale Science and Engineering, University of Kentucky, Lexington, Kentucky 40506, USA

CONTENTS

1. Introduction
2. Theory of AAO Formation
3. Fabrication of AAO Arrays
4. Carbon Nanotubes
5. Metal Nanowires
6. Nanodots
7. Nanoholes
8. Other Devices
9. Summary
Glossary
References

1. INTRODUCTION

The well-organized, self-ordered anodic aluminum oxide (AAO) has emerged as one of the most common structures used in micro- and nanofabrication. This chapter provides a comprehensive review of nanowires, nanodots, nanoholes, and other nanodevices based on AAO structures. The first three sections will review the history and theory of AAO, as well as approaches for processing and fabrication. From Sections 4 to 8, various structures and devices based on AAO will be discussed, including carbon nanotubes (CNTs), metal nanowires, nanodots, nanoholes, and other nanodevices.

1.1. Overview of Aluminum Oxide

Aluminum oxide (Al_2O_3) is one of the most favorable ceramic materials in both industries and laboratories. There are several phases for Al_2O_3, although only three of them are commonly used: α-phase (corundum), γ-phase, and amorphous alumina. The first one is the most thermodynamically stable phase and the second hardest natural mineral known to scientists (four times less hard than diamond) [1]. Nearly all the native alumina ores take the α-phase, such as corundum, ruby (corundum with trace chrome), sapphire (corundum with trace iron and/or titanium), and emery (corundum mixed with considerable other metal oxides, e.g., iron). Bauxite, including clay and kaolin, which is regarded as the most common natural resource of aluminum oxide, is actually a group of composite oxides consisting of alumina, silica, and other metal oxides.

Since α-Al_2O_3 is the form that exists in nature, γ-phase and amorphous oxides are usually prepared artificially through oxidations of metal aluminum. In labs, anodization, in which the metal aluminum serves as the anode and Al atoms lose electrons through the current to turn into Al^{3+}, is one of the most common methods for fabrication of γ-phase and/or amorphous aluminum oxides [2], owing to its low cost and easy control. Lab-produced or commercial γ-Al_2O_3 is always mixed with a huge amount of amorphous Al_2O_3, and its crystalline content is usually quite small. Amorphous Al_2O_3 deposited by anodization or vacuum methods contains a γ-phase to some degree. Al_2O_3 obtained by anodization has some crystalline content, and that by vacuum deposition has no significant peaks except for one broad "hump" in X-ray diffraction (XRD). Owing to this reason, AAO could be considered as a mixture of γ and amorphous phases.

1.2. History of AAO

AAO with hexagonal-shaped pores was first reported in 1953 [3]. Four years later, aluminum oxide films containing regular pore structures were fabricated and verified [4]. The fundamental mechanism for pore formation was proposed in 1959 [5], suggesting that the AAO film grew at the oxide–metal interface. The pores on alumina are ready to trap dyes and pigments. In the last half century, this property is used for color coating, in which a thin and dense oxide layer was formed by anodization on the aluminum surface and then stained with desired colorants [6]. Anodization is also applied on the surface of aluminum alloys as an anticorrosion treatment.

ISBN: 1-58883-160-4

Encyclopedia of Nanoscience and Nanotechnology
Edited by H. S. Nalwa
Volume 11: Pages (235–259)

In 1970, O'Sullivan and Wood [7] presented a model concerning the pore growth of AAO. This model is based on field-assisted dissolution and field-assisted growth of oxide, in which the heterogeneity of Al_2O_3 dissolution is caused and maintained by various electric current densities on different sites on the film. O'Sullivan and Wood's theory was refined later by researchers [8–10]. In the late 1970s, it was found that, in addition to the field-assisted dissolution of Al_2O_3, direct crystallization at the oxide–solution interface is also an important factor for the pore growth [8]. Significant film deposition at the oxide–solution interface was observed in phosphoric acid [9]. Analytical expressions between the pore geometry and the applied voltage were established in the early 1990s [10].

In the 1990s, researchers fabricated well-organized hexagonal pores in large areas by anodization for a long time with refined conditions, especially in oxalic, sulfuric, and phosphoric acids [11, 12]. In 1998, Jessensky et al. [13, 14] proposed a tentative mechanism based on volume expansion to explain the occurrence of the regularity of the pore arrays. In 2005, distinguishable one-dimensional (1D) and horizontally aligned AAO arrays were fabricated by Chen et al. [15, 16]. They also proposed a simple model to explain the phenomena in 1D pore array formation [15]. A similar anodization method has also been applied for fabricating well-aligned pore arrays in other kinds of oxides, for example, self-ordered TiO_2 nanopores obtained by anodization of pure Ti foil [17]. During the last 10 years, low-dimensional nanostructures such as nanotubes [18, 19], nanowires [20], nanodots [21], and nanoholes [22] have been fabricated using hexagonal AAO arrays as templates, masks, and supports. The controllable nanosized pore structure showed great performance for the delivery and separation of biomolecules [23]. In addition, the large and controllable surface area of self-organized AAO provides good sensing capabilities for gases [24, 25].

1.3. Morphologies of AAO

Figure 1 shows a typical scheme of ideally well-defined, self-assembled AAO pore arrays [26]. The pores (a pore along with its hexagonal vicinity is called a "cell") are arranged in a regular-packed hexagonal pattern with a uniform radius, and the spacing between any two pores (or "interpore distance" or "periodicity") is the same. All pores also have a uniform depth. The average number of pores on the unit surface area is called the packing density of the pore array. Between the pore bottom and the aluminum metal layer that has not been anodized, there is an alumina film called the barrier layer.

As we will discuss in Sections 3 and 4, the barrier layer has to be removed in many applications, and the packing density is usually expected to be high, which means small pore diameter and short spacing between the pores. Additionally, the barrier layer is believed to have rectifying property that only allows electronic current to flow from the electrolyte solution to the aluminum metal [27]. This rectifying effect is quite useful in depositing metals on the pore bottom (this issue will be discussed in detail in Section 4.2). In actual cases, the morphologies of the fabricated AAO films are not as perfect as those shown in the above ideal scheme.

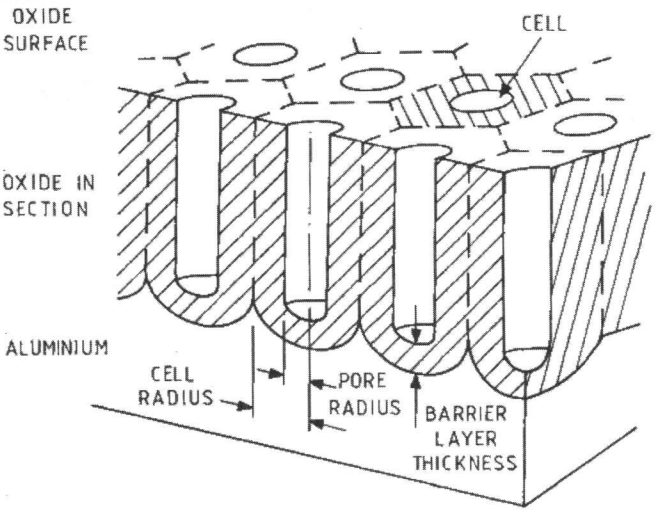

Figure 1. Morphological scheme of the hexagonal AAO pore array. Reprinted with permission from [26], R. C. Furneaux et al., *Nature* 337, 147 (1989). © 1989, Nature Publishing Group.

AAO pore arrays fabricated in early years were not always well organized (Fig. 2a). The excellent regularity and high packing density obtained in recent years (Fig. 2c) should be attributed to the improved anodization methods (see Section 3).

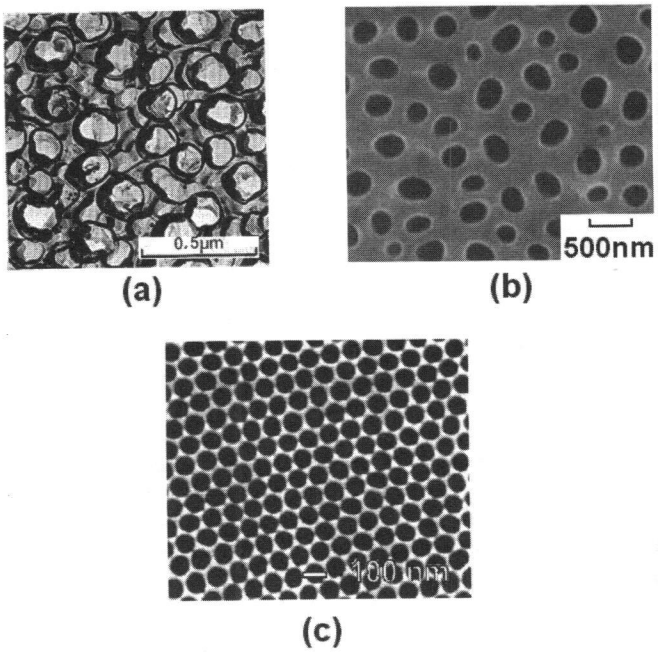

Figure 2. Historical view of surface morphologies of porous AAO films: steady improvement of their regularity. (a) AAO fabricated in 1970. Reprinted with permission from [7], J. P. O'Sullivan and C. G. Wood, *Proc. R. Soc. Lond. Ser. A* 317, 511 (1970). © 1970, The Royal Society of Chemistry. (b) AAO fabricated in 1989. Reprinted with permission from [26], R. C. Furneaux et al., *Nature* 337, 147 (1989). © 1989, Nature Publishing Group. (c) AAO fabricated in 1998. Reprinted with permission from [12], A. P. Li et al., *J. Appl. Phys.* 84, 6023 (1998). © 1998, American Institute of Physics.

2. THEORY OF AAO FORMATION

2.1. Basic Chemistry and Electrochemistry

In the past 50 years, numerous reports and reviews were presented to explain the mechanisms for the growth of AAO films [6–10, 27]. Generally, most researchers agree that the cations and anions in the solution are capable of diffusing through the dense oxide layer. Cations move to the solution–oxide interface, and anions move toward the oxide–metal interface under an applied electric field. This two-way diffusion makes the porous AAO layer grow thicker [6], as shown in Figure 3. Three electrochemical reactions could be expected at the metal–oxide interface: oxidation of Al metal, reduction of proton, and oxidation of oxygen ion. Owing to the large difference in their electrochemical potentials ($O_2/H_2O(H^+) \sim 1.23$V, and $Al^{3+}/Al \sim -1.66$ V) [28], oxidation of O^{2-} or H_2O could hardly happen. Thus, the electrochemical reactions at the metal–oxide interface cause etching of aluminum and bubbling of hydrogen gas. As long as anions (O^{2-}) arrive at the metal–oxide interface, they are neutralized by the newly oxidized Al^{3+} to form insoluble Al_2O_3; thus, the oxide film grows from the bottom (the metal–oxide interface). In the meantime, since the solution is acidic, the surface of the oxide film dissolves. Therefore, as soon as equilibrium between the bottom growth and the surface dissolution is attained, the thickness of the oxide will remain constant, while a significant current still passes through the solution and the anode (Al metal) keeps being oxidized. Although the dissolution usually dominates, the deposition of Al_2O_3 at the solution–oxide interface cannot be neglected. Detailed discussion about this issue will be presented in Section 2.3. Although the model above clarifies the basic chemistry and electrochemistry of AAO growth, it is still very difficult to explain the porous morphology of the film. Next, we will use the field-assisted dissolution model to demonstrate the formation of the pores.

2.2. Field-Assisted Dissolution Model

In Figure 4, at the oxide surface, the Al–O bond is polarized by an applied electric field: the positive part of Al_2O_3, or the Al^{3+} in solid or colloidal state on the film surface, is gradually being "drawn away" to the solution, combining with water molecules to form stable cations; and the negative part (O^{2-}), although being attracted to the bulk oxide by the field, is finally removed by the concentrated hydrogen ions in the acidic solution, because the Al–O bond has been broken.

Figure 5 illustrates the mechanism of pore formation. At the bottom of a pore, the electric field is converged, and thus a high field density is expected; as a result, the rate of the field-assisted dissolution at the pore bottom is faster than in other regions, and the pore is deepened through the anodization process. During the anodization, if a pore is widened, the field convergence is then reduced, and the field-assisted dissolution at the bottom becomes inhabited, the pore will finally be flattened and disappear. In another case, if a pore is initially narrower than average, the intensive electric field at its bottom will cause fast dissolving, and the diameter will become larger. In summary, the diameter of the pore is controlled by the field-assisted dissolution and keeps rather uniformly constant at stable anodization conditions, independent of the anodization time. If the solution composition and temperature remain unchanged through the whole process, the average radius (r) of the pores is simply controlled by the applied bias voltage (U_a). It was verified that the average radius is almost proportional to the applied voltage ($r \sim U_a$), and therefore high voltage causes wide pores [10, 26]. In refined anodization conditions

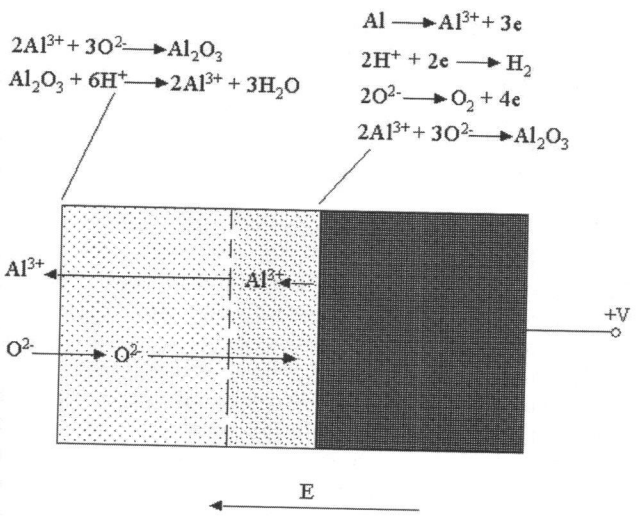

Figure 3. Fundamental chemistry and electrochemistry of AAO growth in acidic solutions. Here, O^{2-} represents any cations in the solution that could be combined with Al^{3+} to form alumina. Actually, in the acidic medium, the concentration of genuine O^{2-} is negligible, and "O^{2-}" used here is just a convenient symbol for various solution anions with negative charges.

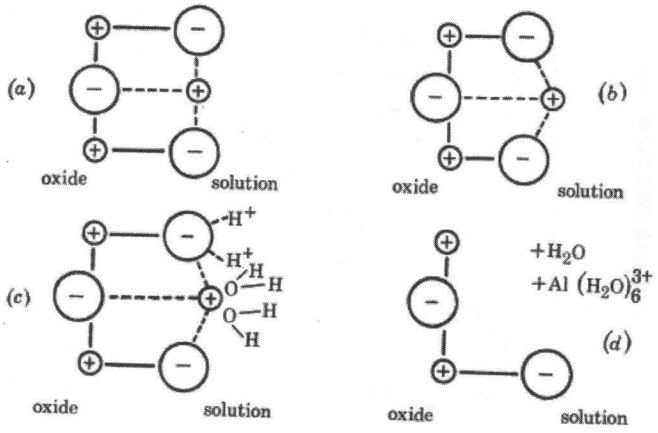

Figure 4. Field-assisted dissolution of Al_2O_3 (a) before polarization, and (b) after polarization; (c) the removal of Al^{3+} and O^{2-} ions; and (d) the remaining oxide. For simplicity, Al_2O_3 is assumed to have a simple NaCl lattice structure. Reprinted with permission from [7], J. P. O'Sullivan and C. G. Wood, *Proc. R. Soc. Lond. Ser. A* 317, 511 (1970). © 1970, The Royal Society of Chemistry.

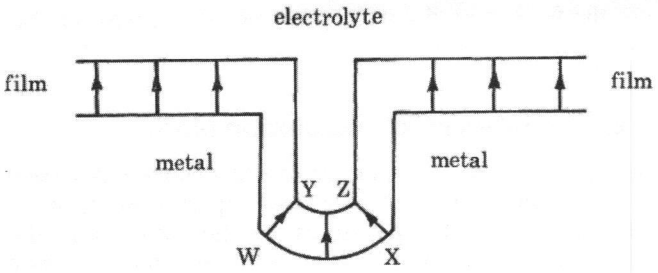

Figure 5. Formation and self-sustaining of pores by field-assisted dissolution. The arrows represent the electric field, which is a vector. Reprinted with permission from [7], J. P. O'Sullivan and C. G. Wood, *Proc. R. Soc. Lond. Ser. A* 317, 511 (1970). © 1970, The Royal Society of Chemistry.

[11–14], under which well-organized hexagonal pore arrays can be achieved, the interpore distance was also found to increase linearly with the bias voltage [12], as shown in Figure 6.

Since the packing density (ρ) is proportional to the reciprocal of the square of the interpore distance ($\rho \sim 1/d^2$) and therefore roughly proportional to $1/U_a^{\ 2}$, doubling the bias voltage causes the packing density to decease with a factor of about $\sqrt{2}/2$. This principle has been applied in fabricating novel shaped structures (see Sections 3.3 and 4.4).

2.3. Oxide Deposition at the Solution–Oxide Interface

While the field-assisted model explained the anodization mechanism quite well, the isotopic tracer method showed that the deposition of Al_2O_3 at the solution–oxide interface was also significant in acidic media [8]; later studies

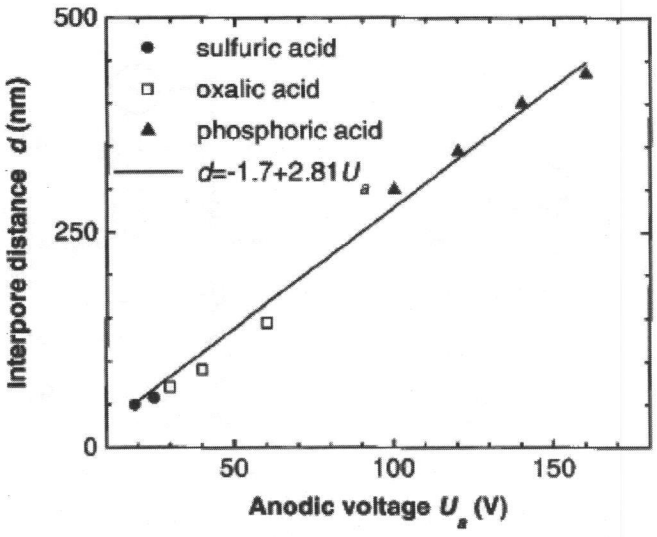

Figure 6. Linear relationship between the interpore distance and applied bias voltage. Three acids – oxalic, sulfuric, and phosphoric acids – were used in experiments. Reprinted with permission from [12], A. P. Li et al., *J. Appl. Phys.* 84, 6023 (1998). © 1998, American Institute of Physics.

proposed a mechanism of field ejection deposition (or direct crystallization) [9], in complement to the field-assisted dissolution process. Figure 7 illustrates the mechanism of the contribution of surface deposition to the formation of the AAO film, in addition to field-assisted deposition. Thicker spots on the oxide film have higher resistance; therefore, the electrical field density at the oxide–solution interface of these thicker spots will become lower than in other regions. As a result, the Al^{3+} concentration beyond those spots will become higher owing to the decrement of the surface electrical field density. In other words, aluminum ions around those high-resistance areas are "less ejected." Therefore the corresponding Al_2O_3 growth rate will get faster than other parts of the film, and these spots will become even thicker. This self-enforcing or self-catalyzing process will finally result in very high "ridges" on the oxide–solution interface, and pores are therefore formed.

The concentration of O^{2-} (or equivalent cations, e.g., HPO_3^{2-} and $C_2O_4^{2-}$) is determined by the bulk solution, which is quite concentrated, compared to the Al^{3+} repulsed from the metal–oxide interface. The anion concentration almost keeps constant everywhere (that is, it is not quite affected by the electrical field). Therefore, the Al_2O_3 deposition process is primarily controlled by the Al^{3+} concentration at the oxide–solution interface.

2.4. Volume Expansion Stress and Self-Organization

While the models in Sections 2.1–2.3 provide detailed principles for the formation of porous AAO films, none of them is able to explain the self-organization that causes the hexagonal regularity of the pores.

An obvious physical change during the anodization of aluminum is the volume expansion, because amorphous Al_2O_3 has a lower density than Al. Therefore, a mechanical stress at the metal–oxide interface is expected, causing repulsive forces among the neighboring pores [13]. According to the literature [12–14], only moderate expansion (tensile force) is able to form pore arrays with high regularity, whereas strong expansion or contraction destroys the delicate self-organization [14]. This is the reason why the well-organized structure can be obtained only by three type of acids (oxalic, sulfuric, and phosphoric) and very narrow voltage ranges for each, or even by two-step anodization (which will be discussed in Section 3.2) [11, 29, 30]. As reported by Li et al. [12], the optimum expansion is about 1.4 times from the metal converting to oxide. A recent study verified the influence of expansion on pore ordering by applying external tensile stress on the film during anodization [31].

However, up to now, the volume expansion mechanism is still a hypothesis. More data and modeling are needed to confirm it. The formation of the hexagonal structure of AAO can be simply explained by close packing of two-dimensional cells [32], as shown in Figure 8. Since the pores ideally take the shape of circles with approximately uniform radii (as discussed in Section 2.3), the packed circles would finally form a repeated hexagon structure, which is the most thermodynamically stable configuration for dense packing, because any two neighboring holes are spaced by

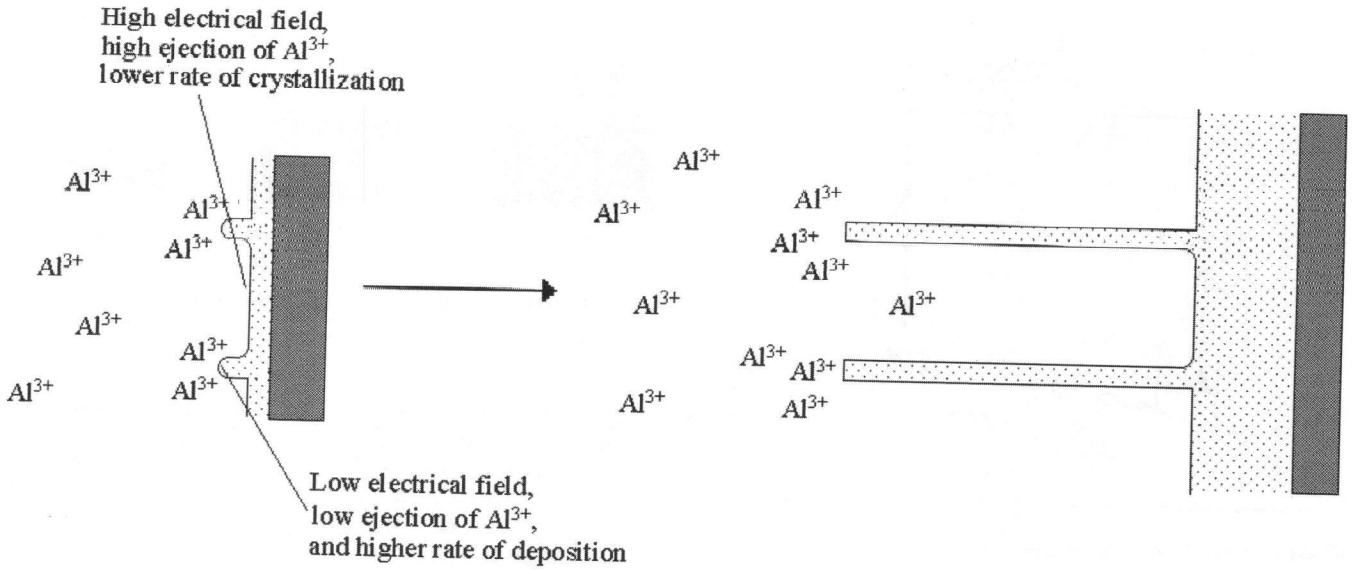

Figure 7. Mechanism for field ejection deposition.

equal distance. This is also the shape of the most regularly ordered structure created by nature, that is, the hive.

3. FABRICATION OF AAO ARRAYS

3.1. Basic Concepts

Similar to most of the other kinds of electrochemical experiments (e.g., electrolysis), the experimental setup of the anodization must include a pair of electrodes (a cathode and an anode), an external circuit to provide power and conduct current, and an electrolyte solution in which the electrodes are immersed in. The aluminum sheet or layer to be anodized, of course, is the anode. The cathode is usually made of inert metals such as platinum. During the anodization, an external voltage is applied to the electrodes by a constant voltage source, and the corresponding current is measured. A typical setup of this two-electrode anodization system is shown in Figure 9. Sometimes a third electrode, the reference electrode (e.g., the calomel electrode), is involved in the anodization system so that the applied bias voltage can be precisely controlled.

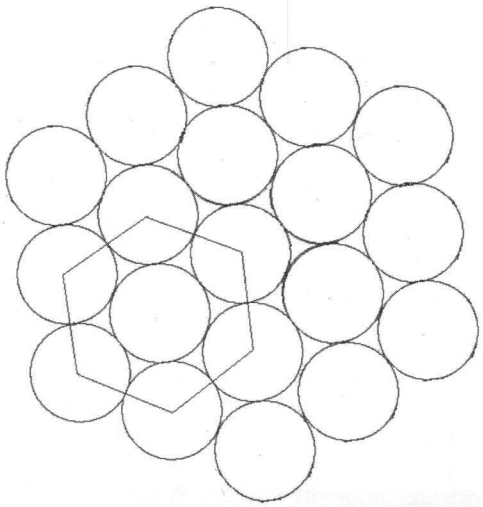

Figure 8. Close packing of two-dimensional cells.

The electrolyte solution is usually acidic, ranging from weak to medium, because the γ-phase or amorphous alumina dissolves very easily and quickly in basic or high-acidic environments. As we have discussed in Sections 1 and 2, up to now, only three acids have been verified to provide well-organized hexagonal pore arrays: oxalic, sulfuric, and phosphoric acids [12]. Therefore, in almost all of the reported research after the mid-1990s, the anodization solution was actually dilution of any one of these three acids [11, 29, 33, 34] or mixtures with other chemical agents [35]. Oxalic acid is the one most frequently chosen in research owing to the medium pore diameter created (~100 nm; see Fig. 6) [11, 13, 15], whereas sulfuric acid is preferred for smaller pores [29, 35].

Anodization voltage is the primary controllable factor in the process, and the magnitude is usually below 50 V in order to obtain pores with small diameters, as we have discussed in Section 2.2. The operation is usually at room temperature [11, 29, 33, 35], while sometimes the solution needs to be chilled to dissipate the heat generated from the electrochemical reactions [34].

3.2. Long-Period Anodization and Two-Step Anodization

As discussed in Section 1.2, well-organized hexagonal AAO pores in large areas were not obtained until the mid-1990s, when refined anodization methods were developed by Masuda et al. [11, 33]. There are two refined methods: long-period anodization and two-step anodization.

Long-period anodization, first reported in 1995 [11], has been used extensively to create well-organized deep

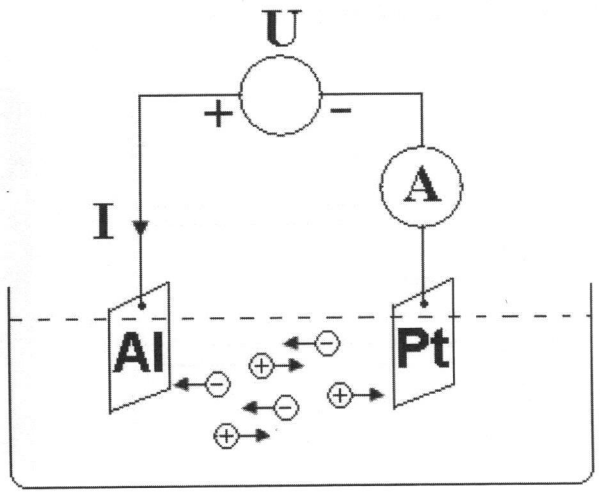

Figure 9. A simple setup for anodization.

pores since then. Compared to fabrication methods used before, under identical conditions (voltage, solution, and temperature, etc.), the anodization time of this process is much longer than what is needed to form alumina of the desired thickness. It is this long time that allows the whole structure to rearrange (or "self-organize") in order to achieve the close-to-ideal hexagonal morphology in large areas (up to square millimeters). Another major characteristic is the selection of anodization conditions. High regularity in a long range only occurs in a very narrow range of process window [11, 29, 30], and as we discussed in Section 2.4, until now, most well-organized AAO pore arrays with midsized to small diameters are based on two groups of anodization conditions. The first group uses a bias voltage of about 25 V in sulfuric acid, resulting in a diameter around 60 nm [29]; and the second one uses a voltage of 40 V and oxalic acid as the electrolyte medium, leading to a diameter of around 100 nm [11]. Large but sparse pores (diameter ~500 nm) with excellent regularity were also fabricated at high voltage up to 195 V in phosphoric acid [34]. These three cases are all included in Figure 6.

Although the principles of the self-organization that causes the hexagonal regularity of the pores remain not very clear (as discussed in Section 2.4), another approach for fabricating highly ordered AAO pore arrays, two-step anodization, was reported just a few months after the publication of the first paper describing long-period anodization [33]. Generally speaking, two-step anodization is based on long-period anodization. The process window is still limited, with only three acids and a narrow range of bias voltage to be chosen. However, it is able to create regular pore array with relatively shallow depth, while the long-period anodization inevitably results in very deep pores. Figure 10 shows the procedure of a typical two-step anodization. The first step is actually a long-period anodization [33, 36], which creates not only the thick porous alumina film but also a well-organized hexagonal texture at the alumina–aluminum interface. After chemically etching away the porous oxide resulting from the first-step anodization, the nanosized concave texture remains, providing a perfect mold for the second-step anodization. Thus, longtime rearrangement of the pores is no

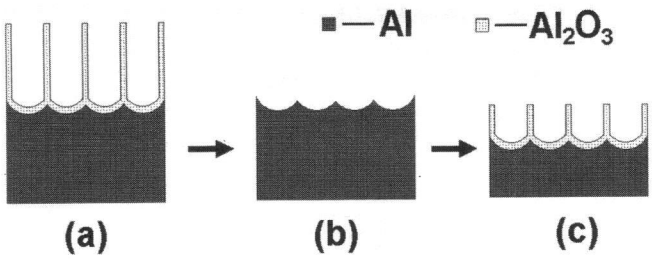

Figure 10. Schematic diagram of a typical two-step anodization.

longer necessary for the second-step anodization because the alumina pores grow from the texture in a quite preorganized pattern. In other words, the pore growth in the second-step anodization does not have to be "self-organized," and a long time is not necessary. Shallows pore arrays are preferably used as shadow masks for the fabrication of nanodots and nanohole arrays, while AAO films with deep pores are excellent templates for the growth of nanosized devices with high aspect ratios, such as CNTs, metal nanowires, and so on. On considering applications, both long-period anodization and two-step anodization are useful in different circumstances.

While self-organized regular morphology of AAO is obtained by appropriate anodization, perfectly ordered pores can be accomplished through a prepatterning process [37, 38]. Followed by anodization, the aluminum metal is molded with a hexagonally ordered array of convexes fabricated by electron beam lithography on a wafer, and the AAO pores will be formed exactly from the molded concaves. Although the patterned SiC wafer [37] or Si_3N_4-spotted Si wafer [38] can be reused as a durable mold so that the throughput would be much higher than that of slow and expensive electron beam lithography, this approach does not have enough flexibility to change or modify the dimensions (e.g., pore diameter) of the array.

3.3. Freestanding AAO Membrane, and Widening and Bifurcating of Pores

Freestanding AAO pores with both ends open are required in many applications (e.g., the AAO mask). To achieve this through-hole pattern, the barrier layer must be removed. Although the thickness of the barrier layer can be reduced to zero by the stepwise decrement of the bias voltage, the diameter of the channel obtained by this approach was in poor uniformity [26]. Another widely used approach in research is described as follows [11, 21, 22, 33, 34, 36, 37]. After anodization, the porous AAO film, along with the aluminum substrate, is immersed in a corrosive medium (e.g., $HgCl_2$ solution) so that the Al metal is selectively etched away. Then, the stripped AAO film is dipped into another etchant (e.g., phosphorus acid) to dissolve its barrier layer. Undoubtedly, the pore diameter becomes larger after this step, because the etchant is corrosive to aluminum oxide. Finally, the through-hole AAO membrane is bonded to a new substrate simply by van der Waals force, as shown in Figure 11. The drawback of this approach is also evident, which is that the small, thin, and vulnerable AAO membrane

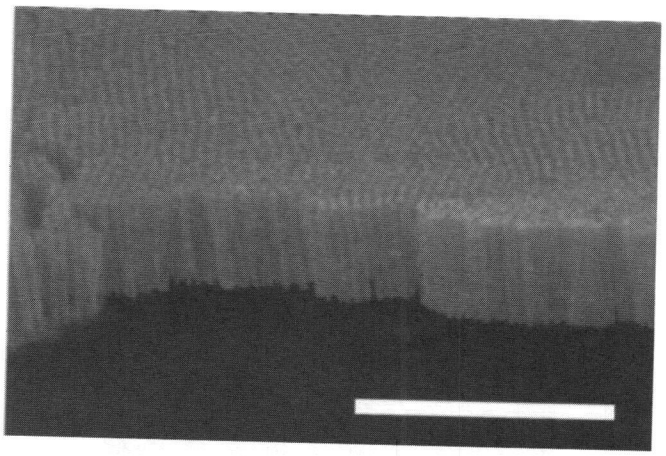

Figure 11. SEM image of an AAO channel membrane on top of a silicon substrate. The light gray part is the AAO membrane, while the dark part is the surface of the Si wafer. The white bar represents 2 μm. Reprinted with permission from [36], W. Nam et al., *Jpn. J. Appl. Phys.* 43, 7793 (2004). © 2004, The Japan Society of Applied Physics.

has to suffer two etching processes. Therefore, the process becomes quite complicated. There are freestanding through-hole AAO membranes commercially available [20].

The linear relationship between the pore diameter and the anodization voltage was discussed in Section 2.2. However, owing to the narrow process window (Sections 2.4 and 3.2), the pore size cannot be easily controlled by the applied bias voltage. Therefore, in order to obtain the desired pore size, a widening process following the anodization becomes necessary. The widening of pores is usually achieved by chemical etching. Phosphorus acid is the most common etchant [35, 37–39]. A longer etching time results in larger pore diameter, and its relationship was found to be quadratic (Fig. 12). During the preparation of freestanding AAO channel membranes, the pore-widening process can be incorporated into the etching of barrier layers [11, 33, 34], and both the widening and etching take place at the same time in the phosphorus acid.

Although it is not quite easy to control the pore diameter directly during anodization, a novel type of array structure was fabricated by changing the bias voltage. In Section 2.2, we have concluded that the packing density (ρ) is roughly proportional to the reciprocal of the square of the bias voltage ($\rho \sim 1/U_a^2$). Therefore, during the anodization, by reducing the voltage to $\sqrt{2}/2$ (or roughly 0.7) times the original value, each pore branches into two individual pores with half of the original pore size, while the already grown part of the original pore still remains [40]. This switching process results in Y-branched pores, as shown in Figure 13. The Y-branched AAO pore array was used for growing Y-junction CNTs (see Section 4.4).

3.4. One-Dimensional AAO Pore Array

Up to now, all discussion has been based on vertically AAO pore arrays, in which the axis of the pore is perpendicular to the substrate. One may imagine a single horizontal array with pores parallel to the substrate surface, as shown in Figure 14. This kind of horizontal, or one-dimensional (1D), array was first reported by Masuda et al. in 1993 by anodizing a sandwich structure of Al_2O_3–Al–glass. However, the pore structures were almost indistinguishable in their scanning electron microscopy (SEM) pictures [41]. Also, a thick Al_2O_3 film and a glass substrate were used as the up and bottom covers of the aluminum to be anodized, and this structure was not compatible with the integrated circuit processes based on silicon.

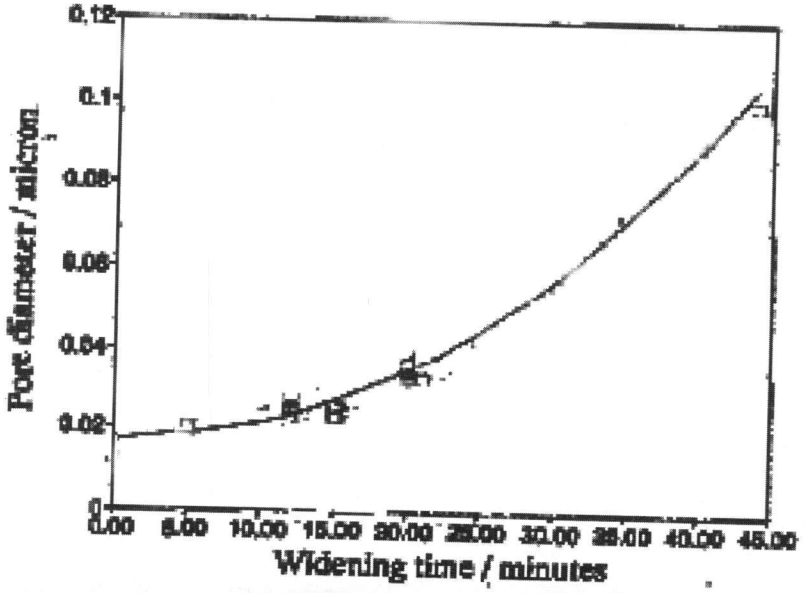

Figure 12. Average pore diameter as a function of widening time. The etchant is 0.085 M phosphorus acid. Reprinted with permission from [39], D. A. Mawlawi et al., *J. Appl. Phys.* 70, 4421 (1991). © 1991, The Japan Society of Applied Physics.

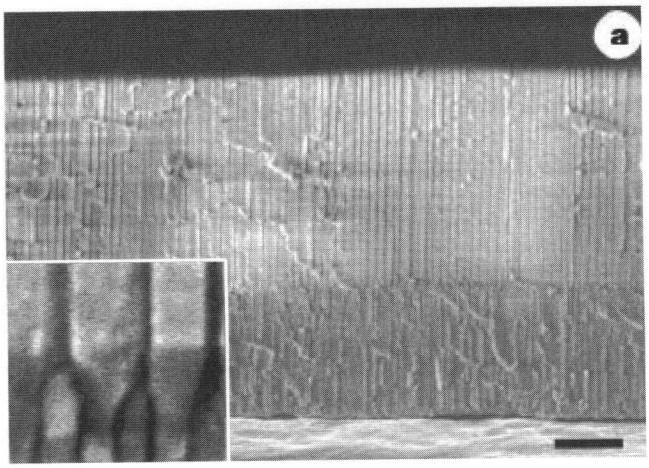

Figure 13. SEM image of Y-branched AAO pore array. Single Y-branched pores can be seen in the lower-left window, where the diameter of the "stem" is about 40 nm and that of the "branch" is 28 nm. The sample was prepared by a two-step anodization, in which the voltage was switched during the second-step anodization. The whole process was carried out in 0.3 M oxalic acid at 10°C. The dark bar represents 1 mm distance. Reprinted with permission from [40], J. Li et al., *Nature* 402, 253 (1999). © 1999, Nature Publishing Group.

There were not any other later reports about well-organized 1D AAO pore arrays until Chen et al. [15, 16] successfully fabricated 1D horizontally aligned pore arrays in 2005. These arrays were achieved from a SiO_2–Al–SiO_2–Si sandwich structure through a modified two-step anodization process in 0.2 M oxalic acid at 40 V bias voltage [15]. As discussed in Section 3.2, the first-step anodization always takes a relatively long time in order to accomplish the self-organization and leave the well-defined pretexture at the alumina–aluminum interface. However, in the horizontal array, since the anodization rate of SiO_2 is much slower than that of Al, the resulting AAO pores would become invisible in the SEM if a large amount of aluminum is anodized in the first step and then dissolves before the second step [15]. Furthermore, cracks were observed after longtime first-step anodization [16]. Owing to these, the anodization time in the first step was shortened to 5 min, while the second step was extended. As a result, clear images with few cracks were obtained (see Fig. 15). Well-organized 1D AAO pore arrays were also fabricated in the SiO_2–Al–Si sandwich structure [16].

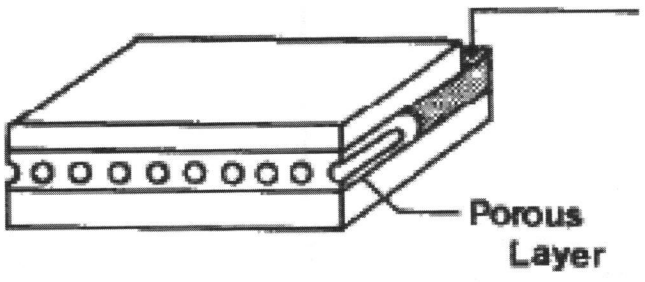

Figure 14. Schematic drawing of a one-dimensional AAO pore array. Reprinted with permission from [41], H. Masuda et al., *Appl. Phys. Lett.* 63, 3155 (1993). © 1993, American Institute of Physics.

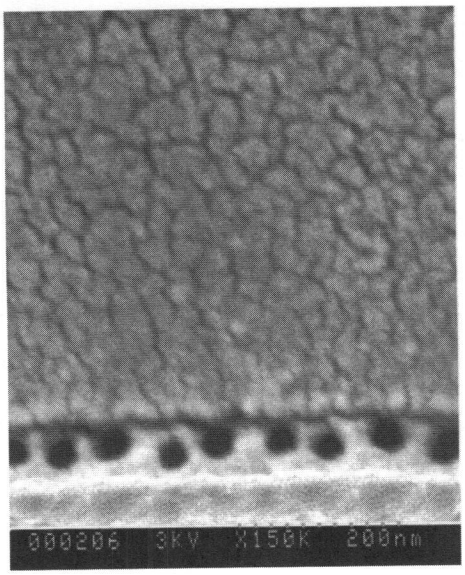

Figure 15. SEM image of a one-dimensional AAO pore array (pore diameter ~40 nm) by a modified two-step anodization. The first step lasted for 5 min, and the second step lasted for 10 min. The brighter regions below and above the pores are silicon dioxide layers. Reprinted with permission from [15], Z. Chen and H. Zhang, *J. Electrochem. Soc.* 152, D227 (2005). © 2005, The Electrochemical Society.

Both structures are compatible with the silicon-integrated circuit processes. Cojocaru et al. [42] also fabricated horizontally aligned AAO pore arrays; this was published in *Nano Letters* in 2005. However, they obtained 3–4 arrays of AAO pores [42], while Chen et al. [15, 16] obtained a single array of AAO pores, which is more useful in the fabrication of nanoelectronic devices. In addition, in Cojocaru et al.'s work, there were hardly any visible pores in the SEM images despite the fact that the images themselves were quite clear with acceptable resolutions [42].

4. CARBON NANOTUBES

The well-defined AAO pore array can be used as a template or a mask, by which other functional nanosized structures or devices, such as CNTs, metal nanowires, nanodots, and nanoholes, can be fabricated. The AAO pore array can also be used for selective binding or immobilization of biomolecules, and as a physical support for gas sensors. The following sections will discuss these devices and structures in detail. In each section, the principles of devices will be described at first in order to gain more understanding, and then the corresponding fabrication approaches will be discussed.

4.1. Introduction to CNTs

The CNT is one of the most interesting nanosized structures synthesized by human beings. Its dimensions and physical properties are controllable through growth and fabrication. Owing to its unique electrical, mechanical, and optical properties, the CNT is also considered one of the most

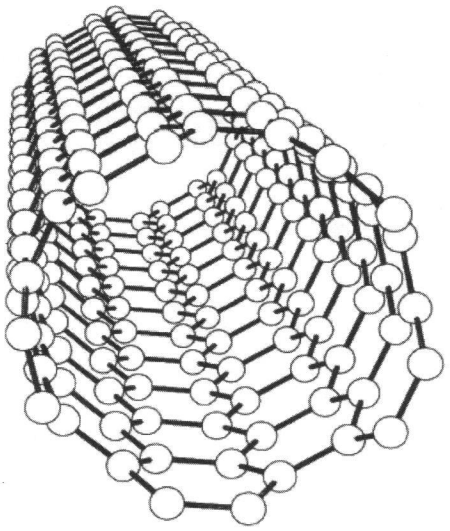

Figure 16. Molecular structure of a SWNT. Reprinted with permission from [44], J. W. Mintmire et al., *Phys. Rev. Lett.* 68, 631 (1992). © 1992, American Physical Society.

attractive synthesized nanostructures [43]. In this section, we will focus on the growth of CNT arrays by using porous AAO as a template, while the principles and history of the CNT will be introduced at the beginning, followed by a discussion of other template-based growth methods in order to compare it with the AAO template-based approach.

Figure 16 shows the molecular structure of a single-wall nanotube (SWNT) [44]. The structure can be simply regarded as a square-shaped atomic sheet of graphite rolled into a seamless cylinder with a diameter of nanometers or even a few angstroms. This atomic assembly is similar to that of C_{60}, a soccer ball–shaped molecule composed of 60 hexagonally linked carbon atoms [45]. Both CNT and C_{60} belong to the fullerene family because of their similarity in bondings. Owing to this, CNTs are also called fullerene tubules [44]. For a multiwalled nanotube (MWNT), the graphene sheet rolls itself into multiple layers, and the top view is like a helix. The detailed structure of a CNT is dependent on the wrapping angle. One may imagine tightly rolling a newspaper with a fixed diameter: the two edges can be joined completely together (i.e., the wrapping angle is 0°) or somewhat missed (i.e., the wrapping angle is over 0°). Different structures result in various physical properties of CNTs [46]. According to the structure-dependent electronic property, CNTs can be roughly divided into two types: metallic and semiconductor. For a semiconducting CNT, its band gap is determined by the wrapping angle as well as its diameter [47]. The synthesis and separation of CNTs with expected physical properties are always major topics in the related research.

The MWNT was discovered in 1991 by Iijima [48]. Two years later, the synthesis of SWNTs was also reported by Iijima et al. [49]. Bethune et al. [50] also independently reported the synthesis of SWNTs. In 1995, Smalley's group functionalized the MWNT into a field emitter, and in the next year they used the tube as a tip for scanning probe microscopy [51, 52]. In 1997, SWNTs were observed to have extraordinary capacity in hydrogen storage [53] and quantum conductance [54]. For the last 10 years, the novel properties of the CNT have been discovered and applied in new areas, such as usually high thermal conductivity [55], superconductivity [56], strain-modified band gaps [57], and optical ignition [58]. In 2001, nanoscaled field effect transistors were fabricated using semiconducting SWNTs as the source-drain channel [59].

4.2. Synthesis of CNT Arrays by Non-AAO Templates

At the time when CNTs were discovered, isolated CNTs were synthesized by arc discharge on graphite electrodes in inert atmospheres [48, 50, 60]. This method was adopted from the synthesis of fullerenes. After that, laser vaporization [61] and chemical decomposition [62, 63] were also developed for the production of CNTs. Since large-scale production of CNTs with good uniformity is always wanted, chemical decomposition (including chemical vapor deposition (CVD) and flame synthesis [63]) undoubtedly has turned out to be the best choice among the above three synthesis methods, owing to its high yield and low cost. Metal particles in the VIII group in the Periodic Table, such as cobalt [50, 61], nickel [61], and iron [62], were always used as the catalysts in chemical decomposition, owing to their long-term reputation in carbonate synthesis.

To synthesize CNTs with high uniformity, controllable growth based on a template is unquestionably a preferable method. Therefore, a template containing numerous aligned nanosized cylindrical channels with adjustable uniform dimensions is necessary. The alignment of CNTs also assists the manipulation and connection necessary for utilizing the CNTs as devices [52, 64]. Furthermore, template-based growth is the easiest and fastest way to produce regularly aligned CNT arrays that are quite useful in electronic devices, such as field emission displays [65]. In 1996, mesoporous silica was chosen as one of the first templates for vertical CNT growth [66, 67]. Nanotubes were synthesized by CVD with iron particles embedded at pore bottoms as catalysts. In the next few years, the large-scale growth of vertical CNT arrays on various substrates, such as glass [68], silicon [69], nickel film [70, 71], and nickel dots on glass [72], was obtained using CVD.

Although CNTs grown on templates (discussed above) did have better uniformity and alignment than those fabricated in the early 1990s, these templates were not controllably well defined with a regular structure, and the resulted alignment was not very satisfying (as shown in Fig. 17a). Although good regularity and alignment of CNTs could be achieved by electron beam lithography [69, 72], either the uniformity was poor (as in Fig. 17b) or the CNTs were actually in bundles [69]. In addition, using electron beam lithography incurs high costs and is time-consuming.

4.3. Vertically Aligned CNT Arrays Grown in AAO Templates

Porous AAO, with its self-ordered regularity and uniformity, was inevitably selected as a template for growing vertically aligned CNTs as early as the mid-1990s [73, 74]. However, the first reported AAO template for CNT growth was not

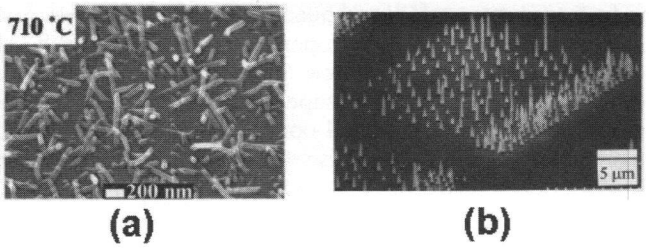

Figure 17. (a) SEM image of CNTs grown on a 4 nm thick nickel film at 710°C. Reprinted with permission from [71], M. P. Siegal et al., *Appl. Phys. Lett.* 80, 2171 (2002). © 2002, American Institute of Physics. (b) SEM image of CNTs grown from nickel nanodots, where the dot array was prepared by electron beam lithography. Reprinted with permission from [72], Z. F. Ren et al., *Appl. Phys. Lett.* 75, 1086 (1999). © 1999, American Institute of Physics.

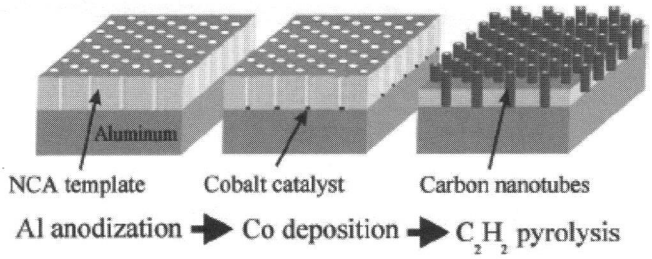

Figure 18. Schematic for growth of vertically aligned CNT arrays in an AAO template. Reprinted with permission from [18], J. Li et al., *Appl. Phys. Lett.* 75, 367 (1999). © 1999, American Institute of Physics.

very good, with pore diameters as large as 260 nm [73]. Facilitated by progress in aluminum anodization, in 1996, fine templates with an average diameter of around 30 nm were fabricated [74]. CNTs based on these AAO templates were synthesized by propylene decomposition at 800°C. The alumina barrier layer was completely removed, and the AAO film was detached from the substrate (an AAO channel membrane with both ends open, as we discussed in Section 3.3). Nonetheless, a nanotube obtained using this method was highly nongraphitized (composed of many tiny localized crystalline domains instead of a single continuous tubule crystal) unless it was annealed at 2800°C [74]. Their size distribution was also quite large. Additionally, this ultrathin plate (50–100 μm) was very vulnerable during manipulations and mechanical operations.

As discussed before, well-controlled bottom-up growth of CNTs in AAO pores can be achieved by catalysis of transition metal particles (iron, nickel, and cobalt) loaded at the bottoms of the pores in the template [66] or just on the substrate [72]. Therefore, these catalysts can also be used for CNT growth in AAO templates. In 1998, CNT arrays were fabricated in porous AAO templates [75] with cobalt as the catalyst, while the size distribution was still large, and the nanotubes were not well aligned. As well-controlled anodization processes became mature (e.g., long-period anodization and two-step anodization, as discussed in Section 3.2), well-aligned CNT arrays with high uniformity were eventually fabricated at the end of the last century [18, 76, 77]. These fabrication processes are quite similar to each other. As shown in Figure 18, an AAO film with well-defined hexagonal pore arrays was prepared. In order to synthesize CNTs with high aspect ratios, deep pores (e.g., 6 μm [18]) were achieved for a very long anodization time. Cobalt particles were then deposited electrochemically at the bottoms of the AAO pores as catalysts. The next step was the synthesis of CNT arrays by high-temperature decomposition of acetylene [18, 77] or ethylene [76]. The chemical decomposition synthesis usually included two steps in the same furnace: first, the cobalt-loaded AAO sample was treated with a reductive gas flow (carbon monoxide [18, 77] or hydrogen [76]) at 500–600°C for a few hours, in order to completely reduce the Co particles. Second, the gas flow was switched to a hydrocarbon gas (acetylene or ethylene, the "source" of the carbon) with a concentration around 2–10% in an inert carrier gas (nitrogen or helium), and then another 1–2 h were needed for the growth of CNTs. The temperature for growth was about 650–800°C.

In order to incorporate the CNTs into Si electronics, the growth of aligned nanotube arrays on silicon substrates is imperative. However, freestanding through-hole AAO membranes on top of silicon wafers (Figure 11) are not reliable templates for CNT growth due to the weak bonding and vulnerability to thermal shocks. Furthermore, AAO on aluminum (as in Fig. 18) was cracked at 300–400°C [76]. One of the solutions to avoid cracks was to use niobium as an alleviating layer [76]. An aluminum film was evaporated on silicon substrate that was already covered with a 100 nm niobium layer and then converted completely into AAO through anodization (Al_2O_3–Nb–Si). The sample was not damaged at 1100°C in helium gas owing to the fact that the thermal expansion coefficient of niobium is close to that of AAO. Unfortunately, the as-grown nanotubes could not be uniformly controlled, and sparse nanotubes were grown [76].

The issue for integration of CNTs into silicon substrates was successfully solved by Hu et al. [19, 35]. Instead of niobium, aluminum was used as the intermediate layer between AAO and silicon, in order to alleviate the thermal tension. The process was rather simple. A 0.5 μm uniform layer of aluminum was evaporated on a silicon substrate and then anodized incompletely. A thin layer of aluminum remained in between the AAO template and the silicon substrate, resulting in a smooth surface without cracks after a high-temperature process. This demonstrated the feasibility of the integration of CNT devices with Si-integrated circuits. The importance of the cobalt catalyst was also studied by Hu et al. [35]. Without cobalt, AAO can only produce nongraphitized CNTs (this is in agreement with early studies, such as Kyotani et al. [74]) because the whole tubule structure does not grow from the bottom but from everywhere in the pore. It is the cobalt that causes well-graphitized bottom-up growth. Also, the existence of cobalt particles at the bottoms of the pore produces hollow structures (as shown in Fig. 19b, the "blank" part between the two sets of walls) from which the CNTs grow. Without cobalt, "solid carbon rods" are likely to be the main product. However, even with catalysis of cobalt, there is still some carbon deposited on the walls of the AAO pores, causing nongraphitized products and compromising the whole uniformity of CNT arrays.

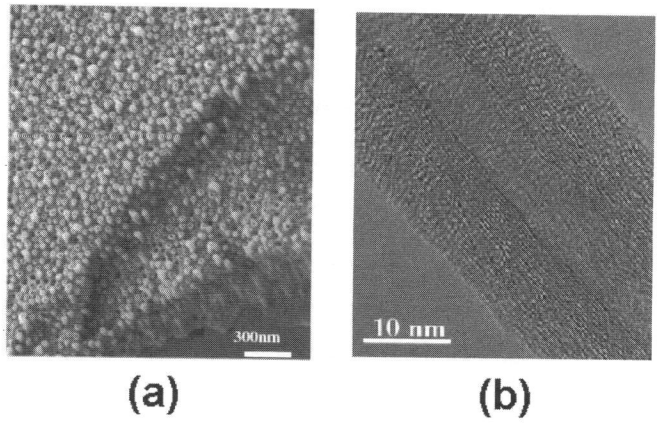

Figure 19. Highly ordered CNT arrays (about 500 nm long) on a silicon substrate using an AAO template. (a) SEM image of the top and side. (b) TEM image of a single CNT in the array, showing multiwalls with an inner diameter of <10 nm. Reprinted with permission from [35], W. C. Hu et al., *J. Nanosci. Nanotech.* 2, 203 (2002). © 2002, American Scientific Publishers.

In order to achieve high-crystalline CNT arrays, optimization of synthesis was studied in recent years [78, 79]. Jeong et al. [78] proposed a detailed mechanism of two competitive depositions inside the pores: one is on the inner walls, mostly amorphous, and the other is on the cobalt particle, resulting in high-crystalline carbon. It was also found that the high yield of crystalline CNTs could be achieved by introducing hydrogen into the deposition reaction [78, 79]. With hydrogen, well-graphitized CNTs even grew over the AAO pores. Additionally, the influence of the concentration of hydrocarbon on the CNT growth was presented [79]. A high hydrocarbon concentration (e.g., over 20%) produces a low filling density of CNTs. This is the reason why low concentrations of acetylene or ethylene were reported in early studies [18, 76, 77]. As the catalyst, the cobalt particles were initially loaded by electroless deposition [76], and later by electrochemical deposition. The pore bottom serves as the cathode, and the deposition current must be alternating (AC) owing to the existence of a nonconductive barrier layer. The AC deposition is also widely applied in nanowire fabrication, and the details will be discussed in the next section. The synthesis method discussed above (hydrocarbon vapor decomposition catalyzed by cobalt particles embedded at the pore bottoms) has been extensively applied in later studies [78–83]. In recent years, well-defined CNT arrays from AAO templates have been used as field emission devices [78–83], as well as transistor arrays [84]. Improvement of uniformity is always the primary purpose of research. Template, substrate, catalyst, and forming gases are all major factors that influence the uniformity.

4.4. Other Types of Aligned CNT Grown in AAO Templates

As we discussed in Section 3.3, bifurcated (Y-branched) AAO pores can be fabricated by switching the anodization

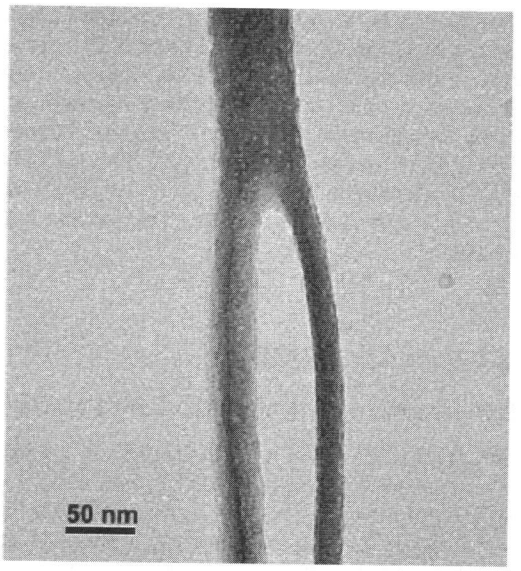

Figure 20. TEM image of a CNT with a Y-junction in a Y-branched AAO template. One may compare this figure with Figure 13. Reprinted with permission from [85], C. Papadopoulos et al., *Phys. Rev. Lett.* 85, 3476 (2000). © 2000, American Physical Society.

voltage to $1/\sqrt{2}$ of the original value. As an immediate result, Y-branched CNTs were fabricated in templates [40]. Since the band gap of a CNT is dependent on the diameter [47], the Y-junction CNT (Figure 20) can be regarded as a two- or three-terminal device with two junctions at each of the connections between the branches and the stem. Diode-like device arrays were fabricated with both branches as one electrode and the stem as the other [85].

After Chen et al. fabricated a 1D AAO pore array (Section 3.4), horizontally aligned CNT arrays in those pores were successfully synthesized by the same research group [86]. Traditionally, horizontally aligned CNTs are achieved by controlled placement [87, 88], which always involves complicated processes. Although back in 1997

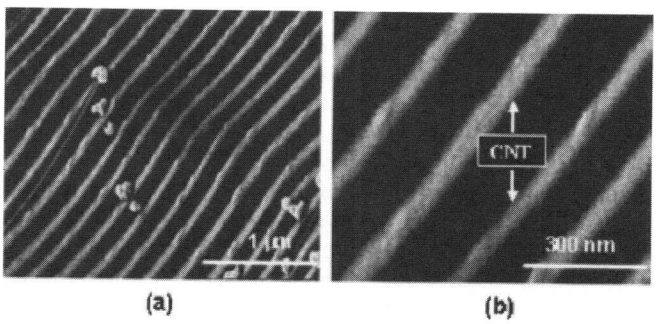

Figure 21. SEM images of a horizontally aligned CNT array grown in a one-dimensional AAO array template. The images were photographed after dissolving all Al metal and oxides. The bright stripes are carbon nanotubes, and the black strips are the substrate. Reprinted with permission from [86], H. Zhang et al., *J. Electrochem. Soc.* 154, H124 (2007). © 2007, The Electrochemical Society.

growth-aligned CNTs were fabricated inside laser-etched linear tracks on silicon substrates, those CNTs were actually entangled in bundles [89]. Later studies demonstrated well-aligned horizontal CNTs by field-directed growth; whereas the density was too low, the average spacing between two neighboring CNTs was around 5 μm [90]. The 1D CNT array (Figure 21) synthesized by Chen's group offers an easy and fast way to fabricate planar electronic and mechanic devices in nanosizes.

5. METAL NANOWIRES

5.1. Introduction to Magnetic Metal Nanowires

Although nanowires have a wide range of applications, such as nanosized semiconductors [91], biomedical sensing [92–93], photoluminescence [94], and molecular circuits [95], the majority of research interest is focused on their capability for storage devices, for example, computer hard disks. Demanding better PCs and MACs requires higher recording density on shrinking disk sizes. Highly ordered magnetic nanowire arrays with each perpendicular and needle-like wire representing a single bit are obviously promising candidates for data storage applications.

Several metal elements, including Ag [96], Au [97], Bi [98], Cd [99], Co [20, 100], Fe [39, 101], Ge [102], Ni [103, 104], Pd [105], Pt [94], and Sn [106], as well as metal alloys [107–111], were made into nanowires in well-ordered hexagonal AAO templates prepared by either two-step anodization or long-period anodization. However, among these arrays, only those made by Fe, Ni, Co, and alloys that contain considerable amount of these three metals stimulate significant interest in the research and manufacturing of storage devices owing to their room temperature ferromagnetic property. Ferromagnetism is the primary characteristic of magnets: the tendency of a metal to remain magnetized after the magnetizing field is withdrawn [112]. For data storage devices, it is necessary and desirable that each recording unit (e.g., a single perpendicular nanowire) keeps its magnetization before rewriting. Therefore, only materials with excellent ferromagnetism, or permanent magnets, such as Fe, Co, Ni, or their alloys, are qualified for storage devices.

Figure 22 shows hysteresis loops of two typical magnets; one is a permanent magnet, and the other is a soft magnet. The loops are plotted by sweeping the applied magnetic strength (H) in one direction and then in the reversed direction (as shown by the arrows in Fig. 22), while observing the change of the magnetic flux density (B) of the materials being magnetized. Permanent magnets have wider and more squarelike loops owing to their strong tendency to remain magnetized. Therefore, two parameters, the coercivity (H_C, the amount of hysteresis, in the unit of Oersted) and remanence (B_R, the magnetization left behind when the applied field becomes zero, in the unit of Tesla), are used to characterize how permanent (or how "hard") a magnet is [113]. Harder magnets have larger H_C and higher B_R. To be used as a permanent magnet, the material must have a strongly oriented magnetic momentum along the expected direction, which means anisotropy, or very different coercivities in various directions [114]. Along a magnet, the direction that spontaneously acquires the highest anisotropy and therefore largest coercivity is called the easy axis, which is mostly determined by two factors: the shape of the bulk and the long-range lattice ordering in microdistance (Weiss domains). Shapes with high aspect ratios usually process large anisotropy, and a more uniform crystal structure generates stronger coercivity along the easy axis. However, when the crystal grain size is very small (<10 nm), superparamagnetism will occur, and the ferromagnetism of the bulk material is gravely reduced. How to avoid and eliminate the superparamagnetism is currently an attractive topic in high-density magnetic storage research [115].

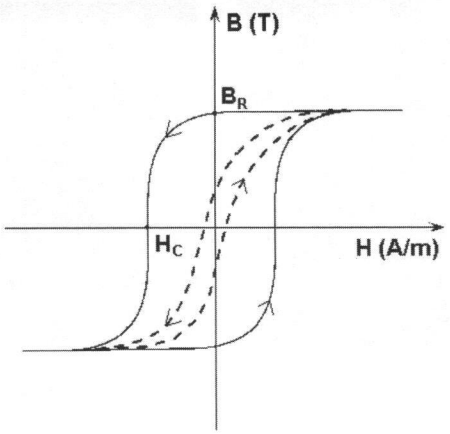

Figure 22. Two typical hysteresis loops. The solid curve represents a permanent ("hard") magnet, and the dashed curve represents a soft magnet.

For perpendicular magnetic storage units, it is definitely desirable that the anisotropic axis of magnetization is perpendicular to the surface of the disk. A magnetic unit with excellent performance must have quite large coercivity and remanence (such as the solid loop in Fig. 22) along the perpendicular direction to reserve the stored information and very weak H_C and B_R (such as the dashed loop in Fig. 22) in parallel to the substrate plane in order to have little influence on the neighboring units. The ultraslim cylindrical shape of a magnetic nanowire with a large aspect ratio already endows the wire with an easy axis, the axial direction perpendicular to the substrate [103]. Furthermore, the tiny wire contains limited Weiss domains, and the radial diameter (10 ~ 100 nm) is not larger than the size of a normal polycrystalline metal grain. Therefore, it is reasonable to assume that a magnetic metal nanowire intrinsically has very strong anisotropy. Nonetheless, superparamagnetism remains a major problem [100, 109], which diverts the expected perpendicular magnetization. Resolutions have been investigated. First, a single metal crystal (or single Weiss domain) with a desired anisotropic axis can be fabricated as nanowires or separate nanosegments (a wire consisting of multiple nanosegments is called a "multilayered nanowire") [103, 108, 110]. Second, the crystal structure of nanowires can be adjusted by alloying and using a multilayered structure so that the undesired horizontal

magnetization becomes weakened [109, 116]. The details for the fabrication of nanowires will be discussed next.

5.2. Fabrication of Metal Nanowires by the AAO Template

In 1993, Huber et al. [117] fabricated metal nanowire arrays by using AAO as a template; the diameter of a single wire is ~200 nm, and the length is ~50 um, with a packing density of 5×10^8 cm^{-2}. One year later, finer magnetic metal (Ni) nanowire arrays were synthesized by electron beam lithography [118]; the wire diameter is around 35 nm, the length is about 120 nm, and the packing density is $\sim 1 \times 10^{10}$ cm^{-2}. With this areal density, a hard disk is able to accommodate 6.5×10^{10} bits (or 65 GB) per square inch. While electron beam lithography showed better results than its AAO template counterpart in the early 1990s, the high cost and low throughput of the former prevent it from being widely used in nanowire fabrication. During the next 13 years, most researchers put their stress on the AAO template [92, 93, 96–111, 116, 119]. Along with progress in the refinement of AAO templates, nanowire structures based on these have greatly improved during recent years, and packing densities no less than 1.0×10^{10} cm^{-2} have been reported [101, 105, 108]. Figure 23 shows Ni–Cu nanowires grown in a self-ordered AAO template in 2002. The packing density reaches 1.1×10^{10} cm^{-2} (or 70 GB/in.^{2}). Since the aspect ratio of nanowires is quite high, the corresponding AAO pore must also be very deep (in Fig. 25, the length of wires is up to 30 μm). Therefore, long anodizing times are usually needed, and the long-period anodization method is also preferred (as discussed in Section 3.2). According to literatures [98, 119], two major kinds of fabrication processes have been developed for the growth of metal nanowires in AAO templates: melt injection (casting) and electrochemical deposition. The former can be regarded as a "pure physical" method without any significant chemical or electrochemical processes.

High-temperature molten metal can be cast into AAO pores either by high gas pressure [98, 117] or by hydraulic force [106]. There are few chemicals involved in this process; therefore, the manipulation complexity is lower than that of electrochemical deposition, and the nonuniformity of the wires that is caused by electrochemical processes is avoided. However, since there is always an aluminum metal layer buried beneath the AAO template in order to alleviate the thermal shock to the AAO film in the melt (as discussed in Section 4.3), the molten metal or alloy must have a melting point lower than that of aluminum (660°C), and this is the reason why the majority of reports of melt injection are focused on metals with very low melting points, such as Bi [98], Sn [106], and Te [117]. Ultrahigh pressure is also needed to overcome the surface tension force in order to push the melt into the ultranarrow AAO channels, which will increase the cost. Additionally, it is nearly impossible to cast multilayered nanowires, which consist of multiple segments of different metals or alloys with distinct borders (as in Fig. 23).

Electrochemical deposition (or electrodeposition) is a typical method for growing metal wires in AAO templates, mostly owing to its low cost. The deposition is usually processed in weak acidic solutions (pH = 2~5). Buffering agents, such as H_3BO_3, are added to the solution to keep the pH value stable. The experimental setup is quite similar to that of anodization (see Section 3.1 and Fig. 9), while the AAO serves as the cathode.

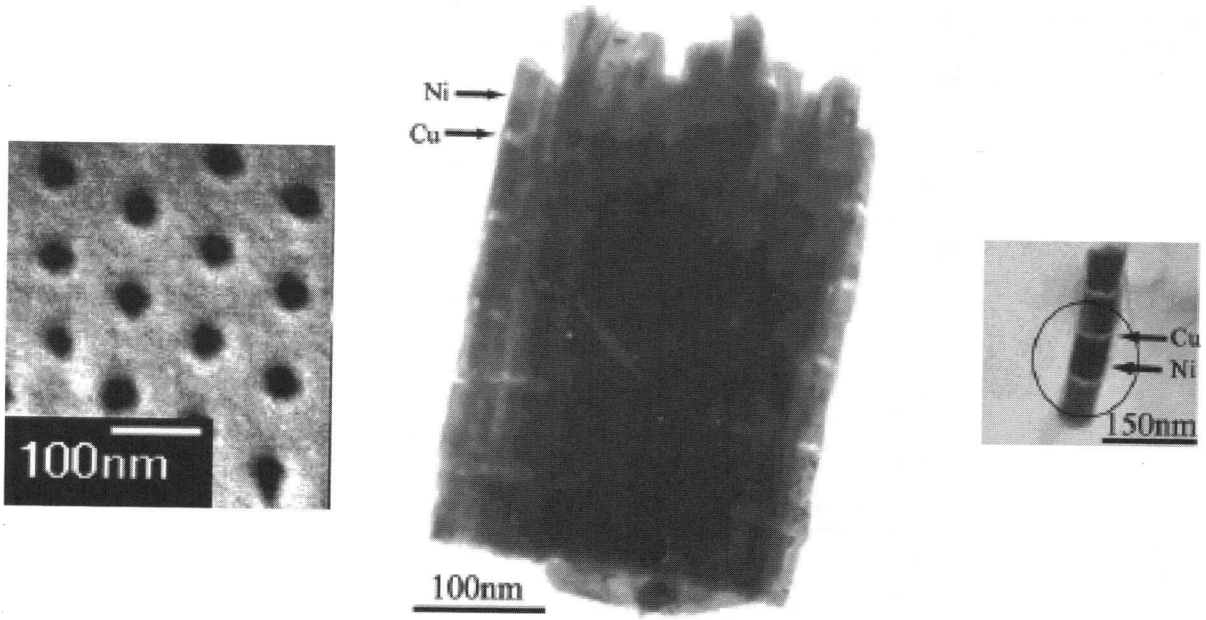

Figure 23. Ordered Ni–Cu nanowire array: SEM image of an AAO template (left), TEM image of a Ni–Cu nanowire bundle (center), and selected-area electron diffraction pattern of a single wire (right). Reprinted with permission from [108], Y. G. Guo et al., *Chem. Mater.* 15, 664 (2003). © 2003, American Chemical Society.

Electrochemical deposition can be simply categorized into two groups: alternating current (AC) deposition and direct current (DC) deposition. Since the barrier layer is an insulator, the applied voltage drops a major part on the layer. Therefore, any thickness fluctuation of the barrier layer causes significant nonuniformity in the deposition in individual pores [119]. Furthermore, the DC bias (~10 V) depletes the metal ions at the oxide–solution interface, resulting in H_2 evolution [120] and other adverse side effects. Fortunately, back in the 1970s, it was found that AC bias was capable of depositing metallic colorants on the rough surface of Al_2O_3 films, with satisfied stability and homogeneity [121]. This effect has been attributed to the rectifying effect of the alumina barrier layer that only allows the cathodic (negative) current to pass through [27, 39, 119]. Since the resistance of AAO along the walls of the pore is so large that the corresponding applied electric field is quite weak, the metal is deposited nowhere but at the pore bottom. The AC deposition method was later widely adopted by researchers for nanowire growth, as well as for the catalyst deposition for CNT growth, as mentioned in Section 4.3.

As shown in Figure 24, during the negative part of the bias, metal ions are reduced and deposited on the AAO pore bottom. Before the depletion of cations close to the bottom surface, the current is switched to positive, in order that the barrier is sufficiently discharged and the defects in the pore bottom are repaired. The deposited metal will not be oxidized because of the absence of anodic (positive) current. A rather long delay time allows the metal ions to supply to the pore bottom. Currently, the AC pulse process is the dominant approach in the electrodeposition of nanowires [96–99, 100–106, 116, 119]. The AC frequency is usually around a few hundred Hertz. Nonetheless, DC deposition is not very uncommon in current research, especially in the fabrication of multilayered nanowires, in which the DC method has an indisputable advantage over its AC counterpart. To accomplish the DC deposition, a conductive layer must be predeposited on the AAO to serve as the cathode. This means that the barrier layer of the template must be completely removed and the AAO array must be freestanding with both ends open. This is the major drawback of the DC method: lab-fabricated through-hole templates are usually not quite mechanically robust and are easily damaged during manipulations. Therefore, researchers sometimes use commercial AAO membranes rather than anodize the aluminum on their own [20, 107]. The detailed processes of etching barrier layers and separating the AAO channel film have been discussed in Section 3.3. The predeposited electrode is usually fabricated by vacuum evaporation methods (E-beam, sputtering, etc.) and composed of chemically inactive metals, such as Au [20, 107] and Ag [108, 109]. This predeposition of electrodes is also applied in the entire pattern transfer of AAO pore arrays (will be discussed in Section 7.3) [11].

Figure 25 shows a cobalt nanowire array prepared from an AAO template [20]. Through electrochemical deposition in $CoSO_4$–H_3BO_3 solution, with a commercially available AAO membrane stick to the cathode (gold), AAO channels were filled with Co metal. After etching away the AAO, a Co nanowire (or nanospike) array standing on the gold electrode was released. As discussed in the Section 5.1, excellent magnetic anisotropy can be obtained from multilayered nanowires, in which a single segment represents a single Weiss domain [108, 110], or an alloy layer with strongly improved anisotropy [109]. As shown in Figure 26 and the picture on the right in Figure 23, a multilayered nanowire usually contains two kinds of segments in an alternating (bamboo-like) pattern: magnetic layers and separation layers. The magnetic segment is composed of ferromagnetic metals or alloys, while the separation layer is filled with nonferromagnetic metals, such as Cu and Pt. To deposit multiple layers, the cathodic potential must be accurately controlled and altered. Therefore, the DC method is necessary in the applications. The bamboo-like structure greatly enhances the anisotropy as well as the absolute coercivity. According to Su et al. [109], the wire in

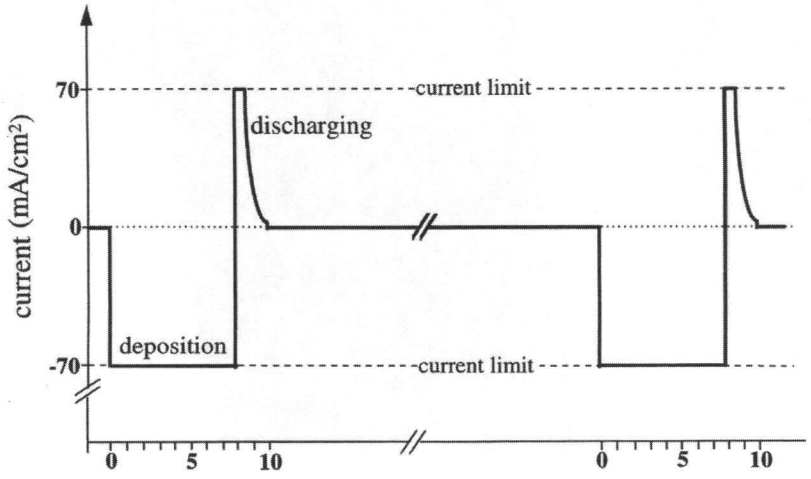

Figure 24. Schematic diagram of electrochemical deposition of Ni into AAO pores by an asymmetric AC pulse current. Deposition of Ni starts at the thinned barrier layer, and the delay time (time between two pulses) varies from 10 ms to 5 s. Reprinted with permission from [119], K. Nielsch et al., *Adv. Mater.* 12, 582 (2000). © 2000, John Wiley & Sons.

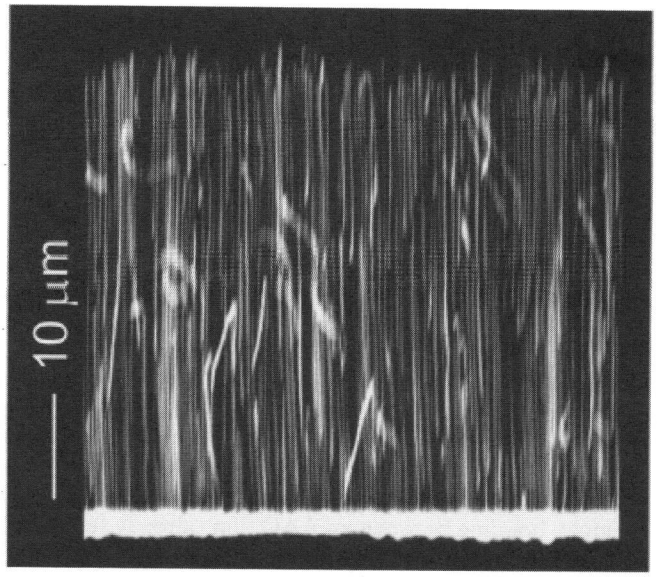

Figure 25. Cross-sectional SEM picture of Co wires fabricated using an AAO template with an average pore diameter of 20 nm and average interpore spacing of 320 nm. The light layer beneath the array was the predeposited gold electrode. Reprinted with permission from [20], G. J. Strijkers et al., *J. Appl. Phys.* 86, 5141 (1999). © 1999, American Institute of Physics.

Figure 26 was found to have a coercivity of 1800 Oersted along the axial direction and a coercivity of 900 Oersted along the radial direction, whereas the nanowire consisting of pure Co had an axial coercivity of about 200 Oersted and the radial H_C was just slightly weaker than the axial. Because it is relatively easy to make a metal cathode layer, DC deposition is also used for nanowires grown in templates prepared by electron beam lithography [118].

6. NANODOTS

Regarding research in metal nanowires, we discussed phenomena and applications of magnetism at the nanoscale. When it comes to nanodot arrays, the principles and applications are mostly related to photoluminescence and photoelectronics.

6.1. From Dimensionless Quantum Boxes to Nanodot Arrays

Like the term nanowire, currently there is no strict definition of the term nanodot. Usually, the word nanowire is used to describe devices with a very large aspect ratio, while a device with a comparable diameter but a very "chubby" shape is likely to be called a nanodot. However, this is neither a strict rule nor one followed by all researchers. A nanodevice with a small but significant aspect ratio (e.g., 8:1 [122] or 5:1 [123]) is rather difficult to categorize into either party. In such cases, nanorod is always a safe term. In this section, the discussion is devoted to planar-shaped nanodots.

Its ultrasmall size and low aspect ratio make the nanodot a good realization of a dimensionless entity, or a quantum box with zero dimension, as long as the size of the real dot is on the order of the Bohr exciton radius (the distance in an electron–hole pair, usually 1 ~ 50 nm) of materials [124]. Fundamental quantum physics revealed that the energy state density ($g(E)$) of a box with ideal zero dimensions is a Dirac delta function (Fig. 27), by which the state density is infinite at the band gap (E_g) and zero elsewhere [125]. Owing to the noticeable quantum effect shown by the nanodot, it is also called a quantum dot. The band gap (E_g) is decided by the size of the nanodot, and there is roughly a linear relationship between E_g and the reciprocal of the square of the diameter of the dot (or d^{-2}, where d is the

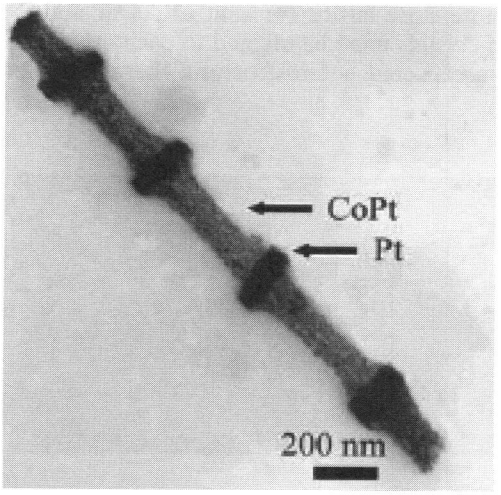

Figure 26. A multilayered nanowire. The dark segment is Pt, and the gray segment is a Co–Pt alloy (55.46% Co and 44.54% Pt). Reprinted with permission from [109], Y. K. Su et al., *Chem. Phys. Lett.* 388, 406 (2004). © 2004, Elsevier.

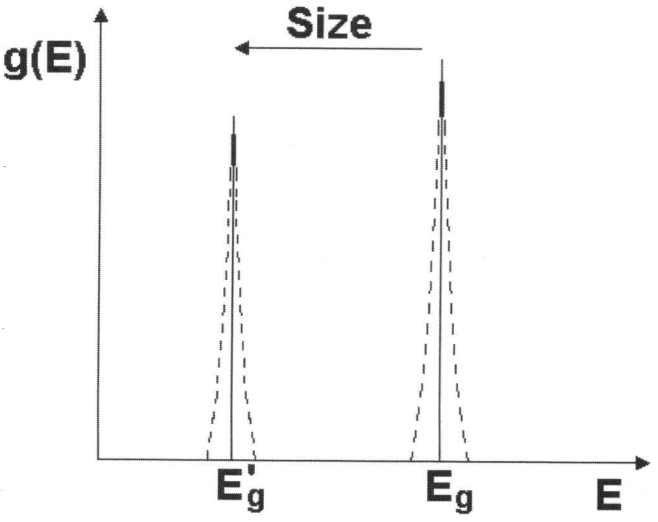

Figure 27. Dirac delta function for the density of states of two dots with different sizes. E_g is the band gap of the smaller dot, while E_g' is that of the larger dot.

diameter) [124, 126, 127]. Shrinking the size leads to higher energy levels [128], as shown in Figure 27. This means that the band gap is easily tunable by changing the size. In other words, a sharp spectrum of photoluminescence (emission, absorption, fluorescence, etc.) with expected wavelength can be obtained by adjusting the diameter of the nanodot through fabrication. For the spectrum from near-infrared (near-IR) to near-ultraviolet (near-UV), the required band gap is from tenths of electron volts to a few electron volts; nanodots in this energy range have been substantially studied [21, 126–142], and the materials involved are mostly semiconductors. Hence, nanodots are promising in photonic applications, such as optical sensors, light emitters and receivers (e.g., the light-emitting diode (LED)) [129], and biological and medicinal fluorescence dyes and tracers [130].

Although a single nanodot would have excellent photonic property in theory, the energy involved is too little to be detected or used. In some fundamental or biological research, certain amounts of nanodots were always dispersed in fluids [128, 130], although for applications in photoelectronic devices, regular nanodot arrays, in which over billions of neighboring dots are closely packed together, are irreplaceably required. For either a flask of dispersed nanodots in some fluid or a close-packed nanodot array, there is always a broadening of the ideal delta function with increase of the size distribution, shown as the dashed curve in Figure 27. Therefore, to make the band sharper so that an ultranarrow spectrum can be obtained, extraordinary uniformity in size is a major consideration in nanodot fabrication.

6.2. Fabrication of Nanodot Arrays

Like other novel nanostructures, fabrication methods for nanodots can be divided into two categories: (1) lithography-related approaches involving procedures such as exposure and development, and (2) approaches based on self-organized nanotemplates. The former includes electron beam lithography [131] and interferometric lithography [132]. The second one includes two kinds of templates, which are commonly used: AAO and polystyrene. Similar to AAO, self-ordered polystyrene with a micro- or nanosized close-packed hexagonal pattern can be achieved by emulsion polymerization, and then used as masks. This method is called nanosphere lithography [133]. Among all the methods mentioned above, electron beam lithography definitely provides the best uniformity and highest controllability in the dot size. However, as discussed previously, it is expensive and slow. The interferometric lithography not only requires a set of laser interference equipment as well as time-consuming procedures such as exposure and development, but also creates very large patterns (~300 nm) [132]. Large pattern creation is undoubtedly a drawback for nanodot fabrication, and the self-ordered spherical hole is at best ~200 nm in diameter [134]. Another major problem for the polystyrene mask is the deformation of the soft polymer thin film, which would even make the patterned holes closed [133, 134].

Over the last few years, porous AAO films have attracted increasing research interest for nanodot fabrication [21, 33, 36, 135–142]. The uniformity of dot arrays can be ensured by a highly self-ordered AAO structure, and it is possible to control the pore diameter and the packing density by controlling anodization conditions and the following pore-widening process. According to references, nanodot arrays fabricated using AAO as a shadow mask usually have a diameter of ~60 nm for each dot, with a spacing of ~100 nm (as shown in Figures 28 and 29). Sharp photoluminescence bands were observed from the template-fabricated nanodot arrays, ranging from near-IR [135] to near-UV [21]. Since the resulting nanodot array must be exposed by etching away the AAO layer, the nanodots cannot be deposited on the bottom of the pores (the alumina barrier layer). Therefore, AAO masks used in nanodot fabrication must be through-hole membranes separated from the original substrate and bonded to a new substrate for the subsequent deposition. Owing to this, a two-step anodization is commonly used in order to achieve a well-defined thin AAO membrane [135, 136, 140, 142]. Etching of the barrier layer and separation of the AAO channel film from the substrate are similar to the steps in the fabrication of nanowires (Section 5.2). For example, bonding between an AAO film (already separated from the original substrate) and smooth silicon [21, 33, 36, 135, 142] or GaAs wafers [136, 137] is realized through van der Waals force (as discussed in Section 3.3). However, the mechanical weakness of freestanding thin AAO membranes remains a primary concern, as mentioned before. Furthermore, the contact at the template–substrate interface must be tight; otherwise, deposition could take place at any possible gaps along the interface.

Vacuum or low-pressure depositions, such as molecular beam epitaxy (MBE) [136, 137], pulsed laser deposition (PLD) [21, 36, 135], plasma-enhanced chemical vapor deposition (PECVD) [138], thermal evaporation [139], electron beam evaporation [33], and sputtering [142], have been used in deposition of nanodot arrays. Generally speaking, for evaporation of nonmetallic materials (usually semiconductors), MBE is a rather conventional method owing to its advantage of growing single-crystal layers. As reported in Mei et al. [136] and Kouklin et al. [137], multilayered InGaAs–GaAs heterostructured nanodot arrays (or quantum well arrays) were fabricated using MBE. InGaAs has a quite close lattice constant to GaAs, and these two types of crystals must be aligned to each other in order to form the expected heterostructure; therefore, the epitaxy

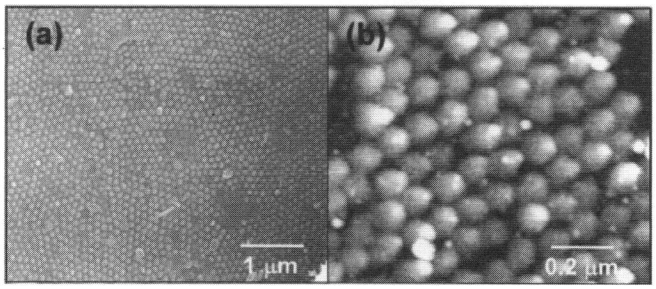

Figure 28. Er-doped Si nanodot array with an average diameter of 60 nm and an interdot distance of 100 nm, fabricated using an AAO channel membrane as an evaporation mask. The array was on a silicon substrate where the AAO was already removed. (a) SEM image; and (b) AFM image. Reprinted with permission from [135], S. M. Park et al., *Appl. Phys. Lett.* 86, 023104/1 (2005). © 2005, American Institute of Physics.

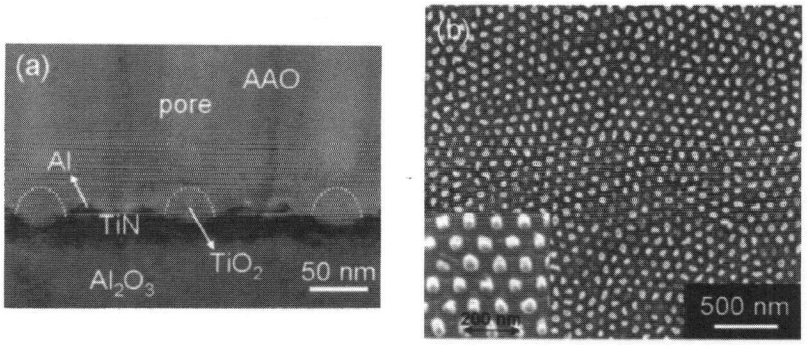

Figure 29. TiO_2 nanodot array fabricated through the anodization of a buried TiN layer, which has an average dot diameter of 60 nm and an interdot spacing of 100 nm. (a) Cross-sectional TEM image; and (b) top-view field emission SEM image where the AAO template was already removed. The inset is a zoomed image of nanodots. Reprinted with permission from [141], P. L. Chen et al., *Appl. Phys. Lett.* 84, 3888 (2004). © 2004, American Institute of Physics.

growth is essentially required. During the last few years, PLD has become a preferable tool for mask deposition of nanodot arrays [21, 36, 135], owing to not only its high efficiency, simple setup, and lack of toxic or explosive gases, but also its ability to produce highly crystalline structures and complex stoichiometry. However, PLD has not yet been reported for the deposition of any complicated dot structures (e.g., the heterojunctioned InGaAs–GaAs) by using the AAO membrane as the mask.

A novel process without separation of an AAO membrane has been reported in Chen et al. [140, 141]. In this method, a conductive titanium nitride (TiN) layer was buried beneath an aluminum film, as long as the Al metal was penetrated by anodization. TiN then started to be anodized, and TiO_2 nanodots were formed at the bottom of each pore. This phase development approach successfully circumvents the difficulty in separation of an AAO membrane from the original substrate. The two-step anodization is not necessarily required. However, this approach needs a special precursor layer (e.g., the buried TiN) that does not react during aluminum anodization, but does react easily in its own anodization. Furthermore, the layer must have good conductivity so that anodization could occur.

AAO mask–based fabrication of nanodot arrays also finds its way into mechanical engineering. Zou et al. [142] reported that a nickel nanodot array with an average diameter of 50 nm and interdot spacing of 100 nm was able to reduce the adhesion forces and friction coefficients of contacting interfaces up to 92% and 83%, respectively. The fabrication process is nearly exactly the same as that in other reports [21, 33, 36, 122, 135, 136]: an AAO channel template was used as a shadow mask on a silicon substrate, and nickel dots were deposited.

7. NANOHOLES

7.1. Nanohole Arrays Used as Photonic Crystals

An AAO template itself is an array of nanoholes, whereas the term nanohole is usually used to describe those fabricated from crystalline semiconductor bulk materials, such as Si [143] or GaAs [22]. The dimensions of these holes are about tens of nanometers in diameter and hundreds of nanometers in depth. In regular arrays, the interhole spacing is about hundreds of nanometers (in Figures 30 and 31, the hole-to-hole distance is around 100 nm). As nanodots demonstrate their potential in photoluminescence and photoelectronics, nanohole arrays are becoming a promising device for photonics. The structure of well-defined nanohole arrays can be considered as a two-dimensional periodic photonic crystal with a constant photonic band gap at all directions on a desired plane, and the size of the periodicity is about half of the wavelength of the photon inhabited by the band gap [22], which means 200–350 nm in the visible range.

The photonic band gap of an optical structure is a specific range of wavelength of electromagnetic wave (light) that is thoroughly not allowable to propagate through the structure. Since this phenomenon is similar to the electronic band gap

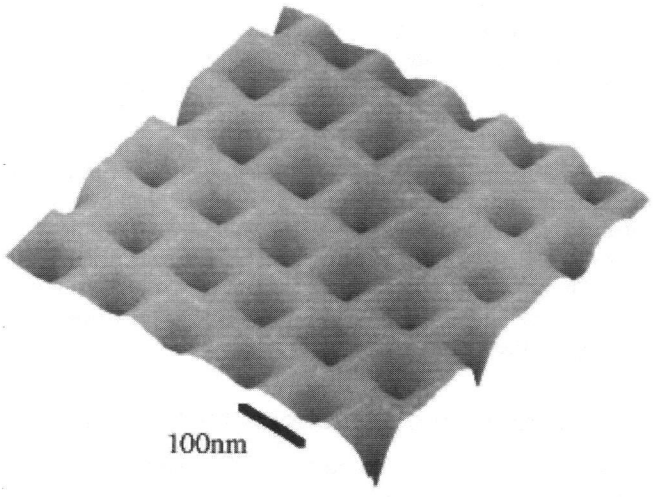

Figure 30. AFM image of the surface of an InP nanohole array, where the AAO mask was removed. Reprinted with permission from [22], M. Nakao et al., *Jpn. J. Appl. Phys.* 38, 1052 (1999). © 1999, The Japan Society of Applied Physics.

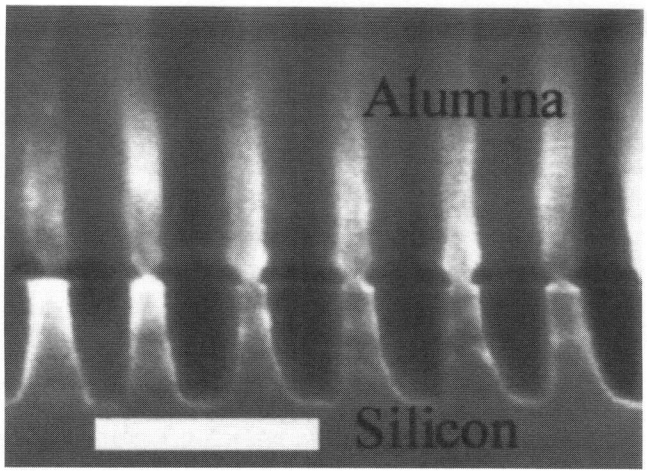

Figure 31. Cross-sectional view of an AAO mask fabricated directly from a desired substrate (Si), and the resulting silicon holes after RIE into silicon for 1 min. The white bar is 200 nm long. Reprinted with permission from [153], D. Crouse et al., *Appl. Phys. Lett.* 76, 49 (2000). © 2000, American Institute of Physics.

in semiconductors, it was therefore named photonic band gap [144]. Any structure with a photonic band gap is called a photonic crystal. The simplest example is a one-dimensional photonic crystal, the Bragg mirror that consists of several layers of two different optical materials deposited in an alternating sequence, where the thickness of each layer is equal to one-quarter of the wavelength of the light expected to be blocked. The band gap of this device was studied nearly 120 years ago by Lord Rayleigh [145]. One-dimensional photonic crystals have been extensively studied and applied in many areas, such as antireflective coating on lenses. However, one-dimensional photonic multilayers are not able to show the expected band gap unless the incident light comes from the normal direction (perpendicular to the multilayered mirror plane). With the development of photonic devices, it is necessary to find photonic crystals with uniform band gaps in two or three dimensions. For an ideal two-dimensional periodic photonic crystal or structure, any in-plane (parallel to the two-dimensional plane) propagation of the photon inside the band gap is completely inhabited [144, 146]. Two- or three-dimensional photonic crystals have been studied and developed during the last 20 years [144, 147–149], and it was found that two-dimensional photonic crystals can be made by drilling a set of micro- to nanosized holes or pitches straightly into a semiconductor plane with equal spacing and high aspect ratios [150, 151]. Therefore, the patterning of a regular array (hexagonal [151]) on the plane and the consequent high-anisotropic deep etching are the key processes for fabrication.

7.2. Fabrication of Nanoholes by AAO Masks

As we have known from studies of other nanodevices, the most common approach to produce periodic patterns is to use electron beam lithography [148, 150, 151]. It has two major drawbacks: high cost and long time. In the last few years, shadow masks based on porous AAO films have turned out to be a quick and low-cost approach for the fabrication of nanohole arrays [22, 38, 143, 152–155]. As mentioned at the beginning of Section 7, the AAO structure itself can also be regarded as a two-dimensional photonic crystal [156], but nanohole arrays based on other materials are needed for the desired optical properties. For a fabrication process, similar to what has been discussed for nanodots, a freestanding, two-end open AAO thin film created through two-step anodization is bonded to the expected substrate by van der Waals force, and then serves as a mask for the subsequent deep etching [22, 143, 152, 153]. The AAO mask is finally removed by chemical etching in order to expose the holes. Whether the sample is masked by an AAO channel film or by a resist pattern created by electron beam lithography, reactive ion etching (RIE) is the most common or even "default" approach for drilling holes into the substrate, owing to the excellent chemical selectivity as well as the high-anisotropic etching profile created by the vertical bombarding ions [22, 38, 143, 150–152]. The hole depth can be up to 1 μm [22]. Nonetheless, the drawback of RIE is also obvious. Owing to the redeposition of nonvolatile materials etched off, the hole becomes narrower as the etching goes deeper. The resulting holes are cone-shaped, and their uniformity is consequently reduced [143]. This phenomenon can be seen in Figure 31, in which the silicon hole is just about 100 nm deep.

Furthermore, as discussed before, separation of the vulnerable thin AAO membrane causes processing failure, and the rebonding to a desired substrate is likely to leave gaps at the bonding interface where unwanted etching would take place. Similar to what has been done in phase-developed nanodot arrays [140], the separation of an AAO membrane was evaded by depositing aluminum metal directly onto a desired semiconductor substrate, and then anodization was processed [153]. After that, the alumina barrier layer was removed, and the substrate is finally mask-etched (Fig. 31). Good conductivity of the substrate is not necessarily required in this method, because the electrical contact can be placed on the front side of aluminum and protected by wax. Nanohole arrays can also be anodized straightly on a substrate masked by an AAO film [154], which is described in detail as follows. A 2 μm aluminum film was deposited on a low-resistivity (0.005–0.01 Ω-cm) p-type silicon wafer by sputtering. Upon the aluminum being completely oxidized by a longtime anodization, silicon areas beneath the bottom of each pore began to be anodized. After removal of the AAO mask (actually, the AAO layer was already collapsed and stripped off during the anodization of silicon), the formed SiO_2 filling in the substrate was dissolved by hydrofluoride acid and the silicon nanohole array was finally released. This method was also used to create GaAs–nanohole arrays (Fig. 32) [155], where the resulting depth is about 50 nm, with a periodicity (interhole distance) of 100 nm. Although the expensive and time-consuming RIE is not involved in this mask anodization approach, the resulting holes are always shallow compared to those by RIE. Therefore, improving the aspect ratio should be a major concern in future research.

7.3. Entire Pattern Transfer

Other than using AAO as an etching mask, nanohole arrays can also be accomplished by entire pattern transfer (Fig. 33),

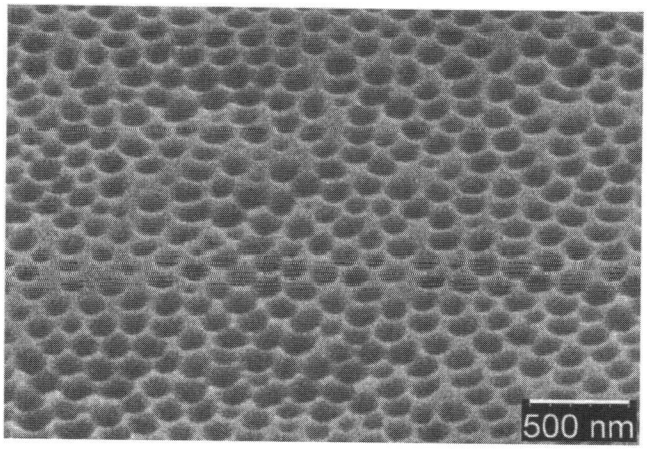

Figure 32. GaAs (nominally undoped) nanohole arrays after anodization for 5 min, where the AAO mask was already removed. Reprinted with permission from [155], K. Meneou et al., *J. Vac. Sci. Technol. B* 23, 1232 (2005). © 2005, American Vacuum Society.

in which the AAO was completely replaced or replicated with other materials by a two-stage molding [11, 157–159]. Three steps are always included in the first stage: separation of a freestanding through-hole AAO membrane, followed by deposition of a thin metal layer on the AAO membrane as electrode or catalyst for the subsequent electrochemical deposition [157–159] or aqueous electroless plating [11], and then a polymer (e.g., poly(methyl methacrylate) (PMMA)) is filled into the pores and a negative print of the AAO array is formed. The second stage is started by removal of the AAO, and a complete negative print of nanoholes on polymer is exposed. This step is followed by electrochemical deposition [157–159] or aqueous electroless plating [11] of desired materials (semiconductors [157–159] or metals [11]), until the polymer negative structure is filled completely. The metal electrode may need to be thickened by electrochemical deposition in order to make a strong support for the semiconductor deposited afterward [157]. Finally, the polymer is removed and a nanohole array with the identical geometry to the original porous AAO membrane is achieved. The approach of the entire pattern transfer was introduced in 1995 [11] and earlier [160], in order to replace the amorphous Al_2O_3 with materials that have much better chemical, mechanical, and thermal stabilities (e.g., Pt and Au), so that the template can be used in harsh processes. However, too many steps are involved in this method, and therefore the throughput is quite low. Furthermore, many semiconductors cannot be deposited by electrochemical deposition or aqueous electroless plating.

8. OTHER DEVICES

8.1. Immobilization, Detection, Separation, Delivery, and Synthesis of Biomolecules

Owing to their high efficiency and low cost, synthetic membranes are widely used in separation, filtration, and selective transport and reaction [161]. Porous AAO films can also be considered as synthetic membranes with a very large

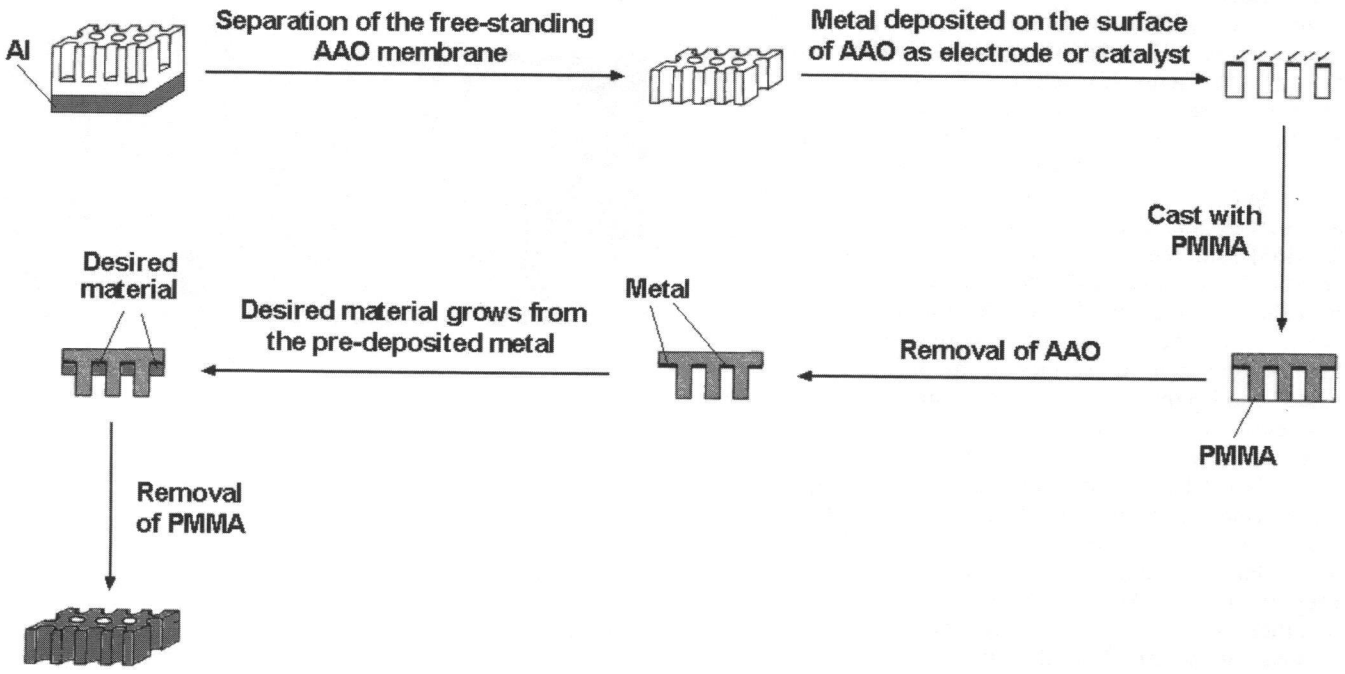

Figure 33. Entire pattern transfer from AAO to a desired material. Reprinted with permission from [11], H. Masuda and K. Fukuda, *Science* 268, 1466 (1995). © 1995, Science.

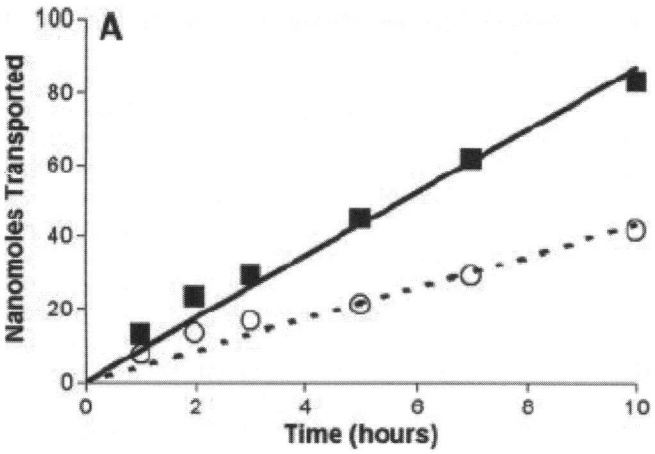

Figure 34. Separation of two enantiomers (a drug named 4-[3-(4-fluorophenyl)-2-hydroxy-1-[1,2,4]triazol-1-yl-propyl]-benzonitrile, with a molecular mass around 322) through an AAO channel membrane (pore diameter ~35 nm) with inner channel walls coated with a thin film of silicon oxide (thickness <3 nm), as well as a very thin layer of enantioselective organic compound (an antibody) on top of silicon. The decorated membrane was mounted between a mixture of the enantiomers and the receiver solution. The plot shows the amount of each enantiomer transported through the membrane. The solid squares and solid line represent the enantiomer that specially binds to the antibody, while the circles and dashed line represent the other enantiomer. The large difference in the transported amounts verifies the enantioselectivity of the antibody–SiO_2–AAO membrane. Reprinted with permission from [23], S. B. Lee et al., *Science* 296, 2198 (2002). © 2002, Science.

relative surface area that is able to be functionalized to selectively attach the desired biomolecules. Current applications include the separation of chiral isomers [23] (Figure 34) and the detection [162, 163], hybridization [164], and delivery of DNAs [165] (Figure 35). Selective binding or immobilization of the biomolecules is always the key step in all the reported works. Since the AAO itself has little selectivity in the absorption of biomolecules, the inner surface of pores has to be modified or decorated. This decoration usually includes a predeposition of another inorganic material (e.g., silica [23, 165]), and then a thin layer of organic compound that is chemically affinitive to the desired biomolecule is imposed over the inorganic film. Sometimes, the organic layer can be directly bonded onto the alumina pore walls [162]. Using this kind of approach, the surface of the porous AAO is "activated" and becomes selective. The same as in many areas of biological studies, fluorescence is the most commonly used method to mark and/or trace the processes [163, 165].

In DNA delivery [165] and hybridization [164], the AAO film is usually used as a template to synthesize the biomolecule carriers. For instance [165], transparent silica nanotubes with a diameter of around 200 nm and a length of 2 μm were prepared in the AAO template through the sol–gel process, and then the inner surface of the tubes was activated. After removal of the template, the dispersed tubes were loaded with the gene segments encoded to express green fluorescence protein. The living cells (monkey kidney COS-7) were then incubated with the DNA-loaded silica tubes. In this case, the DNA-loaded tube behaves like a virus: the tube shell provides an effective shielding for the delivered gene to avoid immune responses from the host cell; and after entering the cell membrane, the loaded DNA is released into the cytoplasm and then expresses green fluorescence protein. As a result, the cells display green color under a microscope. Comparing to the conventional viral delivery, the silica nanotube is nearly nonimmunogenic and causes little toxicity to the cell.

8.2. Support for Hydrogen Sensors

Although palladium (Pd) is the best hydrogen-absorbing material, absorbing up to 900 times its own volume of H_2 at room temperature [28], the response based on the resistance change of bulk palladium to hydrogen is slow, and acceptable response rates can only be obtained at higher H_2 concentrations. Therefore, Pd is always used as a gate metal of metal oxide semiconductor (MOS) sensors, and the sensing principle is not conductivity change but a capacitance–voltage (C–V) shift [166]. In recent years, the improvement of sensing performance (e.g., a much faster, reversible response to low H_2 concentration) of resistive sensors using nanosized Pd structures showed increasing importance [24, 167–169]. Different from the "conventional" sensing principle that palladium increases its resistivity in the presence of hydrogen owing to the formation of palladium hydride [170], some nanostructured Pd sensors were reported to have enhanced conductivity at lower hydrogen concentrations. This "inverse behavior" has been attributed to the break junction effect [167, 171]: a small-sized Pd structure is composed of a lot of

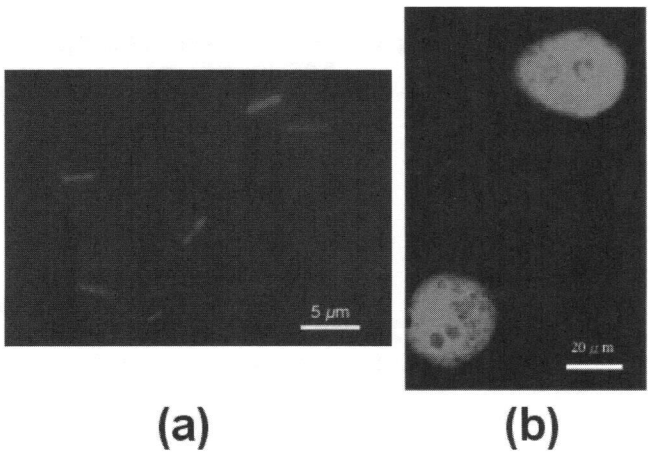

Figure 35. (a) Isolated DNA-loaded silica nanotubes synthesized in an AAO template. The tubes were not introduced into any cells. The green light (displayed as grey-to-white in pictures above because of the color setting) of the tubes was not from any protein but was generated by a DNA stain (SYTO-11) that combined with the loaded gene and emitted fluorescence. (b) Having incubated with DNA-loaded silica tubes, living cells (monkey kidney COS-7) glowed green light, because the delivered DNA was designed for the synthesis of green fluorescence protein. Reprinted with permission from [165], C. C. Chen et al., *Adv. Mater.* 17, 404 (2005). © 2005, John Wiley & Sons.

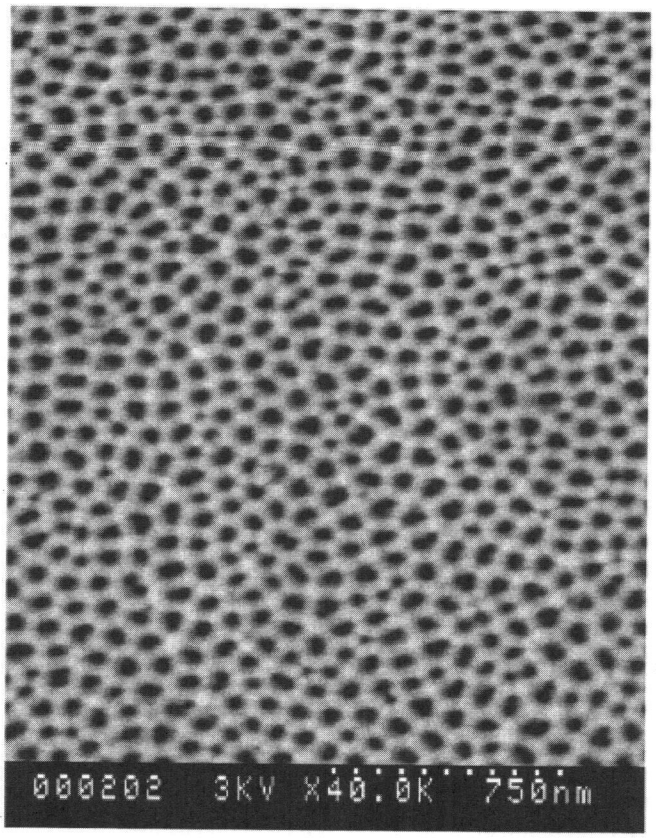

Figure 36. Nanoporous Pd film with a thickness of 45 nm on an AAO substrate prepared by long-period anodization in 0.3 M oxalic acid. Reprinted with permission from [24], D. Ding et al., *Sens. Actuat. B* 120, 182 (2006). © 2006, Elsevier.

discontinuous crystal grains (break junctions), the volume of which expands as hydrogen dissolves into palladium and the grains become partially connected to each other (some junctions are even "closed"); thus, the resistivity decreases at higher H_2 concentrations.

However, blistering and deformation of the Pd films owing to absorption of a large amount of hydrogen are always serious problems that cause erroneous measurements and short lifetimes, especially in the high-concentration range [172]. The above nanostructured palladium is likely to suffer this problem owing to its large relative surface. Even though a palladium–porous-alumina layer was studied for hydrogen gas separation nearly 20 years ago [173], it is not until recently that the well-defined self-assembled AAO film, with a quite large relative surface area, has been used to synthesize a nanostructured palladium sensor for H_2 detection by Ding et al. [24, 168]. Palladium thin films with various thicknesses (45–110 nm, the surface morphology of the 45 nm–thick Pd film on AAO is shown in Figure 36) were deposited on respective AAO substrates by sputtering, and the resistances of the Pd layers were measured at different hydrogen concentration levels. Operating at room temperature, the dynamic range of the sensor is from 250 ppm to 1% hydrogen gas (Fig. 37) with

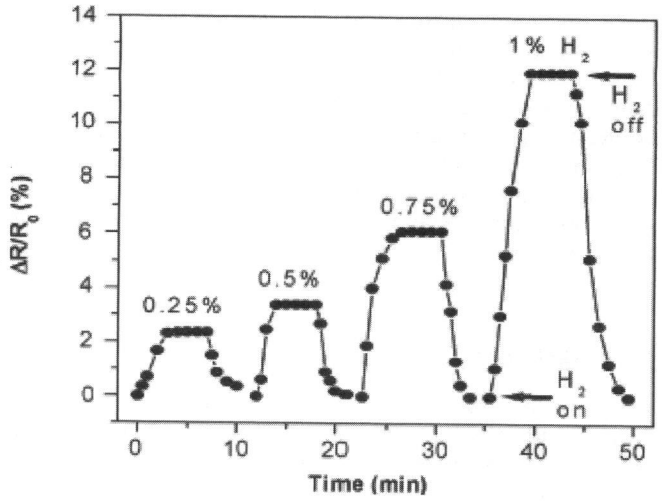

Figure 37. Response of a 45 nm thick Pd film at H_2 concentration levels from 250 ppm to 1% in N_2 background, room temperature; the *y*-axis represents the response in terms of relative change in the resistance. ΔR is the absolute resistance change, and R_0 is the resistance in pure nitrogen. Reprinted with permission from [24], D. Ding et al., *Sens. Actuat. B* 120, 182 (2006). © 2006, Elsevier.

swift and reversible response transients. For the Pd sensors based on porous AAO supporting film, the resistance (R) was found to increase at higher H_2 concentrations. This means the sensing does not depend on the break junction effect. However, the break junction effect does exist in the Pd–AAO sensors as an adverse factor. This is because the cutback of the break junctions at higher H_2 concentration causes a reduction in resistivity and then counteracts the response. As a result, it was found that thicker films (e.g., 110 nm) were likely to have reduced or even zero sensitivity. Therefore, thinner films are preferred in this kind of sensor. As we have mentioned before, for Pd–H_2 sensors, blistering is a problem that misinterprets the measurement and shortens the lifetime. The pinning of metal thin films on the porous AAO support was found to help solve this problem [168]. Since the palladium is deposited on the inside walls of the pores, the whole film is likely to "thrust" into the support, and consequently volume expansion cannot break the structure. With the pinning resulting from the AAO nanoholes, the upper detection limit of the sensor is increased to 10% H_2 concentration without blistering.

Atomic layer deposition (ALD) was reported to be a useful tool for depositing palladium on porous AAO [169]. By ALD, the film thickness is able to be precisely controlled down to a single-atom layer. This indicates an attractive potential of ALD in future research.

8.3. Humidity Sensor

Amorphous or γ-phase Al_2O_3 is one of the most favorable moisture-sensing materials owing to its independence of temperature (25–80°C) at nearly all the range of relative humidity (RH). The impedance of Al_2O_3 decreases with increasing RH [174]. Self-ordered AAO was designed to

make humidity sensors [25]. The sensor was built using well-defined alumina pore arrays formed by anodization in 2 wt. % oxalic acid under 50 V for 2 h. The resulting pore diameter is around 45 nm. An interdigit gold pattern was used as electrodes to measure the impedance change at 5 kHz. The sensing was enhanced by capillary condensation in the nanosized pores. The response of the sensor to cycling transitions between 2% and 45% RH at room temperature is shown in Figure 38.

9. SUMMARY

We have reviewed the fabrication and applications of devices and structures based on self-ordered AAO films, as well as the mechanisms and preparation of AAO itself. With steady progress in AAO fabrication in the last 20 years, well-defined porous alumina structures have become one of the most important templates in the synthesis of nanoscaled devices in large numbers with perfect uniformity. Its accurate controllability of pore diameter with ultrahigh packing density provides an excellent approach for producing nanostructures with low cost. Nanoscaled devices fabricated using AAO are not only useful in practical applications but also of great importance in fundamental studies. The fabricated nanostructures are valuable experimental tools to investigate physical phenomena in the nanoscale, which are quite different from those in the macro world owing to the size effect. Self-ordered AAO pore arrays have been studied extensively since the late 1980s. For example, novel structures such as Y-branched pores and one-dimensional pore arrays have been fabricated. AAO application has also been extended to new areas (i.e., biotechnology). Innovative fabrication techniques (i.e., the phase development approach for nanodot arrays) have also been developed. Finally, we have much better understanding of the physical principles underlying the self-organization of close-packed hexagonal pores (as discussed in Section 2), but still face challenges in understanding new AAO structures such as 1D AAO pore arrays.

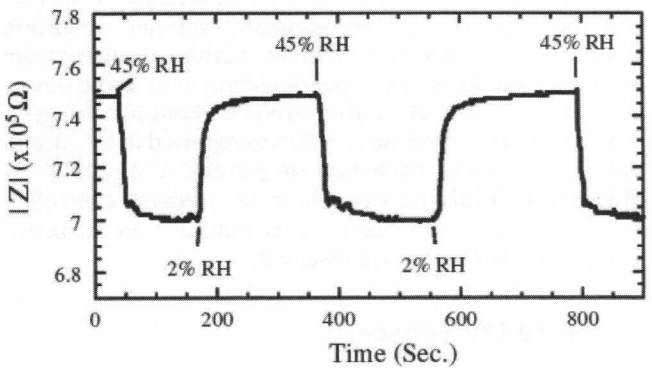

Figure 38. Response of an AAO humidity sensor to cycling transitions between 2% and 45% RH (room temperature). Reprinted with permission from [25], O. K. Varghese et al., *J. Nanosci. Nanotechnol.* 3, 277 (2003). © 2003, American Scientific Publishers.

GLOSSARY

anodization An electrochemical process used to grow oxide on the anode. Electrons are deprived from the anode by the applied voltage, and the surface of the anode is turned into its oxidation state.

anodized aluminum oxide (AAO) Aluminum oxide formed by anodization with aluminum serving as the anode. In this chapter, this term refers to the self-ordered AAO, which contains an hexagonal close-packed array of pores with diameters ranging from a few to hundreds of nanometers. The depth of the pores can be up to tens of micrometers.

carbon nanotube (CNT) One or several graphite sheets that is wrapping together coaxially to form a tubelike material. If it has only one sheet, it is called single-wall nanotube (SWNT). If it has several sheets, it is called a multiwalled nanotube (MWNT).

chemical vapor deposition The formation process of a thin solid film on a substrate (always a semiconductor wafer) by the reactions and/or decompositions of volatile precursors.

DNA delivery A process of introducing foreign DNA into host cells. The combining of single-stranded DNA sequences from two different origins into a hybrid double-stranded DNA is called DNA–DNA hybridization.

electrochemical deposition (electrodeposition) An electrochemical process used to plate layer(s) on the cathode. Cations in the electrolyte are offered electrons and then deposited on the cathode in their reduction states.

electron beam lithography A fabrication approach using an electron beam to create patterns on a substrate. The resolution of the patterns is up to nanometers owing to the low diffraction of electrons. However, the production rate is very slow because the electron beam must be serially scanned across the substrate.

nanodot A nanosized structure with a very low aspect ratio. In this chapter, since the nanodots are fabricated in the AAO template, their shapes are button-like.

nanohole array An array composed of holes with a diameter and interhole distance in the submicrometer size range.

nanowire A nanosized cylindrical structure with a very large aspect ratio.

one-dimensional (1D) AAO pore array A single straight row of AAO pores in which the pore axis is parallel to the substrate surface.

photonic crystal A periodic dielectric structure with a band gap that prohibits the propagation of a certain frequency range of electromagnetic wave (light). The periodicity of a photonic crystal is half of the wavelength of the light to be forbidden. If the periodicity is just at one dimension, then the structure is called a one-dimensional photonic crystal. For two- or three-dimensional photonic crystals, the periodicity is at two or three dimensions, respectively.

relative humidity At a given temperature, the ratio of the partial pressure of water vapor in the ambient to the saturated vapor pressure of water.

ACKNOWLEDGMENT

This work was supported by the National Science Foundation (EPSCOR0447479 and ECS-0609064) and the U.S. Department of Energy (DE-FG26-04NT42171).

REFERENCES

1. W. L. Roberts, T. J. Campbell, and G. R. Rapp, "Encyclopedia of Minerals," New York: Van Nostrand Reinhold, 1990.
2. L. Young, "Anodic Oxide Films," London: Academic Press, 1961.
3. F. Keller, M. S. Hunter, and D. L. Robinson, *J. Electrochem. Soc.* 100, 411 (1953).
4. C. J. L. Booker, J. L. Wood, and A. Walsh, *Br. J. Appl. Phys.* 8, 347 (1957).
5. T. P. Hoar and N. F. Mott, *J. Phys. Chem. Solids* 9, 97 (1959).
6. A. W. Brace, "The Technology of Anodizing Aluminum," Modena, Italy: Interall Srl, 2000.
7. J. P. O'Sullivan and C. G. Wood, *Proc. R. Soc. Lond. Ser. A* 317, 511 (1970).
8. J. Siejka and C. Ortega, *J. Electrochem. Soc.* 124, 883 (1977).
9. L. J. Lanzerotti, W. L. Brown, J. M. Poate, and W. M. Augustyniak, *Nature* 272, 433 (1978).
10. V. P. Parkhutik and V. I. Shershulsky, *J. Phys. D: Appl. Phys.* 25, 1258 (1992).
11. H. Masuda and K. Fukuda, *Science* 268, 1466 (1995).
12. A. P. Li, F. Muller, A. Birner, K. Nielsch, and U. Gosele, *J. Appl. Phys.* 84, 6023 (1998).
13. O. Jessensky, F. Muller, and U. Gosele, *Appl. Phys. Lett.* 72, 1173 (1998).
14. O. Jessensky, F. Muller, and U. Gosele, *J. Electrochem. Soc.* 15, 3735 (1998).
15. Z. Chen and H. Zhang, *J. Electrochem. Soc.* 152, D227 (2005).
16. H. Zhang, Z. Chen, T. Li, and K. Saito, *J. Nanosci. Nanotech.* 5, 1745 (2005).
17. D. Gong, C. A. Grimes, O. K. Varghese, Z. Chen, W. Hu, and E. C. Dickey, *J. Mater. Res.* 16, 3331 (2001).
18. J. Li, C. Papadopoulos, J. M. Xu, and M. Moskovits, *Appl. Phys. Lett.* 75, 367 (1999).
19. W. Hu, D. Gong, and Z. Chen, *Appl. Phys. Lett.* 79, 3083 (2001).
20. G. J. Strijkers, J. H. J. Dalderop, M. A. A. Broeksteeg, H. J. M. Swagten, and W. J. M. de Jonge, *J. Appl. Phys.* 86, 5141 (1999).
21. C. H. Bae, S. M. Park, S. C. Park, and J. S. Ha, *Nanotechnology* 17, 381 (2006).
22. M. Nakao, S. Oku, T. Tamamura, K. Yasui, and H. Masuda, *Jpn. J. Appl. Phys.* 38, 1052 (1999).
23. S. B. Lee, D. T. Mitchell, L. Trofin, T. K. Nevanen, H. Söderlund, and C. R. Martin, *Science* 296, 2198 (2002).
24. D. Ding, Z. Chen, and C. Lu, *Sens. Actuat. B* 120, 182 (2006).
25. O. K. Varghese and C. A. Grimes, *J. Nanosci. Nanotech.* 3, 277 (2003).
26. R. C. Furneaux, W. R. Rigby, and A. P. Davidson, *Nature* 337, 147 (1989).
27. J. W. Diggle, T. C. Downie, and C. W. Goulding, *Chem. Rev.* 69, 365 (1969).
28. D. R. Lide, "CRC Handbook of Chemistry and Physics," 87th ed., Boca Raton, FL: CRC Press, 2006.
29. H. Masuda, F. Hasegwa, and S. Ono, *J. Electrochem. Soc.* 144, L127 (1997).
30. S. Ono, M. Saito, M. Ishiguro, and H. Asoh, *J. Electrochem. Soc.* 151, B473 (2004).
31. G. D. Sulka, S. Stroobants, V. V. Moshchalkov, G. Borghs, and J. P. Celisd, *J. Electrochem. Soc.* 151, B260 (2004).
32. F. H. Kaatz, *Naturwissenschaften* 93, 374 (2006).
33. H. Masuda and M. Satoh, *Jpn. J. Appl. Phys.* 35, L126 (1996).
34. H. Masuda, K. Yada, and A. Osaka, *Jpn. J. Appl. Phys.* 37, L1340 (1998).
35. W. Hu, L. Yuan, Z. Chen, D. Gong, and K. Saito, *J. Nanosci. Nanotech.* 2, 203 (2002).
36. W. Nam, H. Seo, S. C. Park, C. H. Bae, S. W. Nam, S. M. Park, and J. S. Ha, *Jpn. J. Appl. Phys.* 43, 7793 (2004).
37. H. Masuda, H. Yamada, M. Satoh, H. Asoh, M. Nakao, and T. Tamamura, *Appl. Phys. Lett.* 71, 2770 (1997).
38. J. Zou, X. Qi, L. Tan, and B. J. H. Stadler, *Appl. Phys. Lett.* 89, 093106/1 (2006).
39. D. A. Mawlawi, N. Coombs, and M. Moskovits, *J. Appl. Phys.* 70, 4421 (1991).
40. J. Li, C. Papadopoulos, and J. Xu, *Nature* 402, 253 (1999).
41. H. Masuda, K. Nishio, and N. Baba, *Appl. Phys. Lett.* 63, 3155 (1993).
42. C. S. Cojocaru, J. M. Padovani, T. Wade, C. Mandoli, G. Jaskierowicz, J. E. Wegrowe, A. F. I. Morral, and D. Pribat, *Nano Lett.* 5, 675 (2005).
43. Z. Chen, "Encyclopedia of Nanoscience and Nanotechnology: Nanotubes for Nanoelectronics," Valencia, CA: American Scientific Publishers, 2004.
44. J. W. Mintmire, B. I. Dunlap, and C. T. White, *Phys. Rev. Lett.* 68, 631 (1992).
45. W. Kratschmer, L. D. Lamb, K. Fostiropoulos, and D. R. Huffman, *Nature* 347, 354 (1990).
46. N. Hamada, S. Sawada, and A. Oshiyama, *Phys. Rev. Lett.* 68, 1579 (1992).
47. J. W. G. Wildoer, L. C. Venema, A. G. Rinzler, R. E. Smalley, and C. Dekker, *Nature* 391, 59 (1998)
48. S. Iijima, *Nature* 354, 56 (1991).
49. S. Iijima and T. Ichihashi, *Nature* 363, 603 (1993).
50. D. S. Bethune, H. Klang, M. S. de Vries, G. Gorman, R. Savoy, J. Vazquez, and R. Beyers, *Nature* 363, 605 (1993).
51. A. G. Rinzler, J. H. Hafner, P. Nikolaev, L. Lou, S. G. Kim, D. Tomanek, P. Nordlander, D. T. Colbert, and R. E. Smalley, *Science* 269, 1550 (1995).
52. H. J. Dai, J. H. Hafner, A. G. Rinzler, D. T. Colbert, and R. E. Smalley, *Nature* 384, 147 (1996).
53. A. C. Dillon, K. M. Jones, T. A. Bekkendahl, C. H. Kiang, D. S. Bethune, and M. J. Heben, *Nature* 386, 377 (1997).
54. S. J. Tans, M. H. Devoret, H. Dai, A. Thess, R. E. Smalley, L. J. Geerligs, and C. Dekker, *Nature* 386, 474 (1997).
55. S. Berber, Y. K. Kwon, and David Tomanek, *Phys. Rev. Lett.* 84, 4613 (2000).
56. M. Kociak, A. Y. Kasumov, S. Gueron, B. Reulet, I. I. Khodos, Y. B. Gorbatov, V. T. Volkov, L. Vaccarini, and H. Bouchiat, *Phys. Rev. Lett.* 86, 2416 (2001).
57. E. D. Minot, Y. Yaish, V. Sazonova, J. Y. Park, M. Brink, and P. L. McEuen, *Phys. Rev. Lett.* 90, 156401/1 (2003).
58. P. M. Ajayan, M. Terrones, A. de la Guardia, V. Huc, N. Grobert, B. Q. Wei, H. Lezec, G. Ramanath, and T. W. Ebbesen, *Science* 296, 705 (2002).
59. P. G. Collins, M. S. Arnold, and P. Avouris, *Science* 292, 706 (2001).
60. T. W. Ebbesen and P. M. Ajayan, *Nature* 358, 220 (1992).
61. T. Guo, P. Nicolaev, A. Thess, D. T. Colbert, and R. E. Smalley, *Chem. Phys. Lett.* 243, 49 (1995).
62. M. J. Yacaman, M. M. Yoshida, L. Rendon, and J. G. Santiesteban, *Appl. Phys. Lett.* 62, 657 (1993).
63. L. Yuan, K. Saito, W. Hu, and Z. Chen, *Chem. Phys. Lett.* 346, 23 (2001).
64. S. S. Wong, E. Joselevich, A. T. Woolley, C. L. Cheung, and C. M. Lieber, *Nature* 394, 52 (1998).

65. W. B. Choi, D. S. Chung, J. H. Kang, H. Y. Kim, Y. W. Jin, I. T. Han, Y. H. Lee, et al., *Appl. Phys. Lett.* 75, 3129 (1999).
66. W. Z. Li, S. S. Xie, L. X. Qian, B. H. Chang, B. S. Zou, W. Y. Zhou, R. A. Zhao, and G. Wang, *Science* 274, 1701 (1996).
67. W. Li, H. Zhang, C. Wang, Y. Zhang, L. Xu, K. Zhu, and S. Xie, *Appl. Phys. Lett.* 70, 2684 (1997).
68. Z. F. Ren, Z. P. Huang, J. W. Xu, J. H. Wang, P. Bush, M. P. Siegal, and P. N. Provencio, *Science* 282, 1105 (1998).
69. S. Fan, W. Liang, H. Dang, N. Franklin, T. Tombler, M. Chapline, and H. Dai, *Physica E* 8, 179 (2000).
70. Z. P. Huang, J. W. Xu, Z. F. Ren, and J. H. Wang, *Appl. Phys. Lett.* 73, 3845 (1998).
71. M. P. Siegal, D. L. Overmyer, and P. P. Provencio, *Appl. Phys. Lett.* 80, 2171 (2002).
72. Z. F. Ren, Z. P. Huang, D. Z. Wang, J. G. Wen, J. W. Xu, J. H. Wang, L. E. Calvet, J. Chen, J. F. Klemic, and M. A. Reed, *Appl. Phys. Lett.* 75, 1086 (1999).
73. R. V. Parthasarathy, K. L. N. Phani, and C. R. Martin, *Adv. Mater.* 7, 896 (1995).
74. T. Kyotani, L. Tsai, and A. Tomita, *Chem. Mater.* 8, 2109 (1996).
75. J. Li, M. Moskovits, and T. L. Haslett, *Chem. Mater.* 10, 1963 (1998).
76. T. Iwasaki, T. Motoi, and T. Den, *Appl. Phys. Lett.* 75, 2044 (1999).
77. J. S. Suh and J. S. Lee, *Appl. Phys. Lett.* 75, 2047 (1999).
78. S. H. Jeong, H. Y. Hwang, S. K. Hwang, and K. H. Lee, *Carbon* 42, 2073 (2004).
79. P. L. Chen, J. K. Chang, C. T. Kuo, and F. M. Pan, *Appl. Phys. Lett.* 86, 123111/1 (2005).
80. Z. H. Yuan, H. Huang, H. Y. Dang, J. E. Cao, B. H. Hu, and S. S. Fan, *Appl. Phys. Lett.* 78, 3127 (2001).
81. J. S. Suh, K. S. Jeong, J. S. Lee, and I. Han, *Appl. Phys. Lett.* 80, 2392 (2002).
82. S. H. Jeong and K. H. Lee, *Jpn. J. Appl. Phys.* 43, L1106 (2004).
83. W. J. Yu, Y. S. Cho, G. S. Choi, and D. Kim, *Nanotechnology* 16, S291 (2005).
84. W. B. Choi, J. U. Chu, K. S. Jeong, E. J. Bae, J. W. Lee, J. J. Kim, and J. O. Lee, *Appl. Phys. Lett.* 79, 3696 (2001).
85. C. Papadopoulos, A. Rakitin, J. Li, A. S. Vedeneev, and J. M. Xu, *Phys. Rev. Lett.* 85, 3476 (2000).
86. H. Zhang, Z. Chen, T. Li, F. Wang, and K. Saito, *J. Electrochem. Soc.* 154, H124 (2007).
87. Y. H. Yan, S. Li, L. Q. Chen, M. B. C. Park, and Q. Zhang, *Nanotechnology* 17, 5696 (2006).
88. S. M. Jung, J. Hahn, H. Y. Jung, and J. S. Suh, *Nano Lett.* 6, 1569 (2006).
89. M. Terrones, N. Grobert, J. Olivares, J. P. Zhang, H. Terrones, K. Kordatos, W. K. Hsu, et al., *Nature* 388, 52 (1997).
90. Y. Zhang, A. Chang, J. Cao, Q. Wang, W. Kim, Y. Li, N. Morris, E. Yenilmez, J. Kong, and H. Dai, *Appl. Phys. Lett.* 79, 3155 (2001).
91. D. Wang, Q. Wang, A. Javey, R. Tu, H. Dai, H. Kim, P. C. McIntyre, T. Krishnamohan, and K. C. Saraswat, *Appl. Phys. Lett.* 83, 2432 (2003).
92. F. Qu, M. Yang, G. Shen, and R. Yu, *Biosens. Bioelectron.* 22, 1749 (2007).
93. L. Liu, N. Jia, Q. Zhou, M. Yan, and Z. Jiang, *Mater. Sci. Eng. C* 27, 57 (2007).
94. J. K. Lee, W. K. Koh, W. S. Chae, and Y. R. Kim, *Chem. Commun.* 2002, 138 (2002).
95. L. Kim, J. Kim, G. H. Gu, and J. S. Suh, *Chem. Phys. Lett.* 427, 137 (2006).
96. R. Yang, C. Sui, J. Gong, and L. Qu, *Mater. Lett.* 61, 900 (2007).
97. Z. Wang and M. Brust, *Nanoscale Res. Lett.* 2, 34 (2007).
98. Z. Zhang, D. Gekhtman, M. S. Dresselhaus, and J. Y. Ying, *Chem. Mater.* 11, 1659 (1999).
99. D. A. Mawlawi, C. Z. Liu, and M. Moskovits, *J. Mater. Res.* 9, 1014 (1994).
100. H. Zeng, M. Zheng, R. Skomski, and D. J. Sellmyer, *J. Appl. Phys.* 87, 4718 (2000).
101. D. Routkevitch, A. A. Tager, J. Haruyama, D. A. Mawlawi, M. Moskovits, and J. M. Xu, *IEEE Trans. Elec. Dev.* 43, 1646 (1996).
102. D. Erts, B. Polyakov, B. Daly, M. A. Morris, S. Ellingboe, J. Boland, and J. D. Holmes, *J. Phys. Chem. B* 110, 820 (2006).
103. K. Nieisch, R. B. Wehrspohn, J. Barthel, J. Kirschner, U. Gosele, S. F. Fischer, and H. Kronmuller, *Appl. Phys. Lett.* 79, 1360 (2001).
104. A. J. Yin, J. Li, W. Jian, A. J. Bennett, and J. M. Xu, *Appl. Phys. Lett.* 79, 1039 (2001).
105. K. T. Kim, S. J. Sim, and S. M. Cho, *IEEE Sens. J.* 6, 509 (2006).
106. C. C. Chen, Y. Bisrat, Z. P. Luo, R. E. Schaak, C. G. Chao, and D. C. Lagoudas, *Nanotechnology* 17, 367 (2006).
107. P. R. Evans, G. Yi, and W. Schwarzacher, *Appl. Phys. Lett.* 76, 481 (2000).
108. Y. G. Guo, L. J. Wan, C. F. Zhu, D. L. Yang, D. M. Chen, and C. L. Bai, *Chem. Mater.* 15, 664 (2003).
109. Y. K. Su, D. H. Qin, H. L. Zhang, H. Li, and H. L. Li, *Chem. Phys. Lett.* 388, 406 (2004).
110. H. P. Liang, Y. G. Guo, J. S. Hu, C. F. Zhu, L. J. Wan, and C. L. Bai, *Inorg. Chem.* 44, 3013 (2005).
111. W. Li, G. A. Jones, Y. Peng, T. H. Shen, and G. Hill, *J. Appl. Phys.* 97, 104306/1 (2005).
112. R. M. Bozorth, "Ferromagnetism," New York: IEEE Press, 1993.
113. J. D. Livingston, *J. Appl. Phys.* 52, 2544 (1981).
114. C. Kittel, "Introduction to Solid State Physics," New York: John Wiley, 1996.
115. D. Weller and A. Moser, *IEEE Trans. Magn.* 35, 4423 (1999).
116. S. Shiomi, T. Nishii, and H. Kohama, *IEEE Trans. Magn.* 38, 2568 (2002).
117. C. A. Huber, T. E. Huber, M. Sadoqi, J. A. Lubin, S. Manalia, and C. B. Prater, *Science* 263, 800 (1994).
118. S. Y. Chou, M. S. Wei, P. R. Krauss, and P. B. Fischer, *J. Appl. Phys.* 76, 6673 (1994).
119. K. Nielsch, F. Müller, A. P. Li, and U. Gösele, *Adv. Mater.* 12, 582 (2000).
120. D. G. W. Goad and M. Moskovits, *J. Appl. Phys.* 49, 2929 (1978).
121. W. Sautter, G. Ibe, and J. Meier, *Aluminium* 50, 143 (1974).
122. H. Chik, J. Liang, S. G. Cloutier, N. Kouklin, and J. M. Xu, *Appl. Phys. Lett.* 84, 3376 (2004).
123. S. W. Shin, S. G. Lee, J. Lee, C. N. Whang, J. H. Lee, I. H. Choi, T. G. Kim, and J. H. Song, *Nanotechnology* 16, 1392 (2005).
124. P. N. Prasad, "Nanophotonics," New York: John Wiley, 2004.
125. Bart Van Zeghbroeck, "Principles of Semiconductor Devices," Boulder: University of Colorado, 2002.
126. J. B. Xia, *Phys. Rev. B* 40, 8500 (1989).
127. V. V. Nikesh, A. D. Lad, S. Kimura, S. Nozaki, and S. Mahamuni, *J. Appl. Phys.* 100, 113520/1 (2006).
128. L. T. Canham, *Appl. Phys. Lett.* 57, 1046 (1990).
129. S. Coe, W. K. Woo, M. Bawendi, and V. Bulovic, *Nature* 420, 800 (2002).
130. R. E. Bailey, A. M. Smith, and S. Nie, *Physica E* 25, 1 (2004).
131. A. Chen, S. J. Chua, P. Chen, X. Y. Chen, and L. K. Jian, *Nanotechnology* 17, 3903 (2006).
132. S. C. Lee, K. J. Malloy, and S. R. J. Brueck, *J. Appl. Phys.* 90, 4163 (2001).
133. M. Winzer, M. Kleiber, N. Dix, and R. Wiesendanger, *Appl. Phys. A* 63, 617 (1996).
134. P. Wu, L. Peng, X. Tuo, X. Wang, and J. Yuan, *Nanotechnology* 16, 1693 (2005).
135. S. M. Park, C. H. Bae, W. S. Nam, S. C. Park, and J. S. Ha, *Appl. Phys. Lett.* 86, 023104/1 (2005).
136. X. Mei, D. Kim, H. E. Ruda, and Q. X. Guo, *Appl. Phys. Lett.* 81, 361 (2002).

137. N. Kouklin, H. Chik, J. Liang, M. Tzolov, J. M. Xu, J. B. Heroux, and W. I. Wang, *J. Phys. D: Appl. Phys.* 36, 2634 (2003).
138. H. Hu and D. He, *Mater. Lett.* 60, 1019 (2006).
139. T. Shimizu, M. Nagayanagi, T. Ishida, O. Sakata, T. Oku, H. Sakaue, T. Takahagi, and S. Shingubara, *Electrochem. Solid-State Lett.* 9, J13 (2006).
140. P. L. Chen, C. T. Kuo, T. G. Tsai, B. W. Wu, C. C. Hsu, and F. M. Pan, *Appl. Phys. Lett.* 82, 2796 (2003).
141. P. L. Chen, C. T. Kuo, F. M. Pan, and T. G. Tsai, *Appl. Phys. Lett.* 84, 3888 (2004).
142. M. Zou, H. Wang, P. R. Larson, K. L. Hobbs, M. B. Johnson, and O. K. Awitor, *Trib. Lett.* 24, 137 (2006).
143. S. Shingubara, O. Okino, Y. Murakami, H. Sakaue, and T. Takahagi, *J. Vac. Sci. Technol. B* 19, 1901 (2001).
144. E. Yablonovitch, *Sci. Am.* 285, 47 (2001).
145. J. W. S. Rayleigh, *Philos. Mag.* 26, 256 (1888).
146. R. D. Meade, K. D. Brommer, A. M. Rappe, and J. D. Joannopoulos, *Appl. Phys. Lett.* 61, 495 (1992).
147. E. Yablonovitch, *Phys. Rev. Lett.* 58, 2059 (1987).
148. T. F. Krauss, R. M. De La Rue, and S. Brand, *Nature* 383, 699 (1996).
149. P. Lodahl, A. F. van Driel, I. S. Nikolaev, A. Irman, K. Overgaag, D. Vanmaekelbergh, and W. L. Vos, *Nature* 430, 654 (2004).
150. C. C. Cheng, A. Scherer, R. C. Tyan, Y. Fainman, G. Witzgall, and E. Yablonovitch, *J. Vac. Sci. Technol. B* 15, 2764 (1997).
151. T. Baba, N. Kamizawa, and M. Ikeda, *Physica B* 227, 415 (1996).
152. Q. Guo, T. Tanaka, M. Nishio, H. Ogawa, X. Mei, and H. Ruda, *Jpn. J. Appl. Phys.* 41, L118 (2002).
153. D. Crouse, Y. H. Lo, A. E. Miller, and M. Crouse, *Appl. Phys. Lett.* 76, 49 (2000).
154. H. Asoh, M. Matsuo, M. Yoshihama, and S. Ono, *Appl. Phys. Lett.* 83, 4408 (2003).
155. K. Meneou, C. L. Tsai, Z. H. Zhang, and K. Y. Cheng, *J. Vac. Sci. Technol. B* 23, 1232 (2005).
156. H. Masuda, M. Ohya, H. Asoh, M. Nakao, M. Nohtomi, and T. Tamamura, *Jpn. J. Appl. Phys.* 38, L1403 (1999).
157. P. Hoyer, N. Baba, and H. Masuda, *Appl. Phys. Lett.* 66, 2700 (1995).
158. P. Hoyer, *Langmuir* 12, 1411 (1996).
159. K. Jiang, Y. Wang, J. Dong, L. Gui, and Y. Tang, *Langmuir* 17, 3635 (2001).
160. H. Masuda, H. Tanaka, and N. Baba, *Chem. Lett.* 19, 621 (1990).
161. P. Meares, "Membrane Separation Processes," New York: Elsevier, 1976.
162. I. Vlassiouk, A. Krasnoslobodtsev, S. Smirnov, and M. Germann, *Langmuir* 20, 9913 (2004).
163. S. G. Cloutier, A. D. Lazareck, and J. M. Xu, *Appl. Phys. Lett.* 88, 013904/1 (2006).
164. J. P. Lellouche, S. Govindaraji, A. Joseph, J. Jang, and K. J. Lee, *Chem. Commun.* 2005, 4357 (2005).
165. C. C. Chen, Y. C. Liu, C. H. Wu, C. C. Yeh, M. T. Su, and Y. C. Wu, *Adv. Mater.* 17, 404 (2005).
166. I. Lundstrom, S. Shivaraman, C. Svensson, and L. Lundkvist, *Appl. Phys. Lett.* 26, 55 (1975).
167. T. Xu, M. P. Zach, Z. L. Xiao, D. Rosenmann, U. Welp, W. K. Kwok, and G. W. Crabtree, *Appl. Phys. Lett.* 86, 203104/1 (2005).
168. D. Ding and Z. Chen, *Sens. Lett.* 4, 331 (2006).
169. J. W. Elam, G. Xiong, C. Y. Han, H. H. Wang, J. P. Birrell, U. Welp, J. N. Hryn, et al., *J. Nanomater.* 2006, 64501/1 (2006).
170. B. M. Geerken and R. Griessen, *J. Phys. F: Met. Phys.* 13, 963 (1983).
171. F. Favier, E. C. Walter, M. P. Zach, T. Benter, and R. M. Penner, *Science* 293, 2227 (2001).
172. M. Armgarth and C. Nylander, *IEEE Elec. Dev. Lett.* 3, 384 (1982).
173. M. Konno, M. Shindo, S. Sugawara, and S. Saito, *J. Membrane Sci.* 37, 193 (1988).
174. Z. Chen and C. Lu, *Sens. Lett.* 3, 274 (2005).